Politecnico di Milano

School of Industrial and Information Engineering

Master of Science in Nuclear Engineering

Predictive simulations of Deuterium Fuelling in DTT Plasma

Supervisor:
prof. Matteo Passoni

Supervisor:
dott. Paola Mantica

Master thesis of:
Lorenzo Aucone
920551

ACADEMIC YEAR 2020/2021

Contents

List of figures

List of tables

Riassunto

Al giorno d'oggi, la ricerca sulla fusione termonucleare controllata gioca un ruolo cruciale nella transizione energetica verso le fonti rinnovabili. In questo contesto si colloca DTT (Divertor Tokamak Test facility), un reattore sperimentale pensato per studiare lo scarico controllato di energia e particelle convogliandoli in una particolare struttura chiamata divertore.

Per raggiungere buone prestazioni di plasma, sarà necessario bilanciare la perdita continua di particelle con sistemi di fuelling esterni, al fine di mantenere costanti i livelli di densità. In particolare, dato che DTT non è stato pensato per operare la fusione tra deuterio (D) e trizio (T), l'iniezione di particelle dall'esterno coinvolgerà solamente il primo isotopo.

Al fine di studiare ed ottimizzare i 2 principali metodi di fuelling previsti per DTT, gas puff e iniezione di pellets, è necessario un lavoro di simulazioni predittive riguardanti sia queste sorgenti di particelle che la risposta del plasma ad esse. Questa tesi si inserisce in questo specifico ambito di ricerca.

La prima parte del lavoro ha avuto lo scopo di stabilire il livello nominale di gas puff da applicare per sostenere la densità di plasma desiderata, al fine di valutare se questo supera i limiti di fattibilità del sistema di pompaggio e anche i livelli oltre i quali si avrebbe un degradamento del bordo del plasma. I risultati hanno messo in luce dei valori molto vicini o anche superiori a quelli critici, a seconda della scelta dei parametri di bordo del plasma.

Si è quindi reso necessario un lavoro di simulazioni predittive con lo scopo di studiare l'iniezione di pellets come metodo di fuelling alternativo. In particolare, si è esplorata la possibilità di rifornire il plasma utilizzando pellets di tre diverse dimensioni e velocità (1: r=0.7mm, v=617m/s; 2: r=1mm, v=516m/s; 3: r=1.3mm, v=640m/s). I risultati ottenuti hanno mostrato che pellets di dimensioni contenute ($r \leq 1$mm) costituiscono un'ottima alternativa al gas puff, in quanto riescono a sostenere i livelli di densità desiderati senza produrre perturbazioni eccessive e con frequenze ottimizzate ben

in linea con le capacità degli iniettori disponibili.

Abstract

Controlled thermonuclear fusion plays a crucial role in the energy transaction towards renewable sources. In this context is placed DTT (Divertor Tokamak Test facility), an experimental reactor designed to study the controlled exhaust of energy and particles by conveying them to a particular structure called divertor.

In order to keep constant the density levels and to obtain good plasma performance, it is necessary to balance the continuous particle losses with external fuelling systems. In particular, since DTT is not meant to operate the fusion between Deuterium (D) and Tritium (T), the supply of particles from outside will involve only the first isotope.

In order to study and optimize the two fuelling systems for DTT, gas puff and pellet injection, predictive simulations concerning both particle sources and the plasma response to them are required. The first part of this thesis work consists of a series of simulations establishing the nominal level of gas puff which has to be applied to sustain the desired plasma density. This procedure is needed to evaluate if this value exceeds the feasibility limits of the pumping system and the levels beyond which plasma edge degradation would occur. The results shows values that are very close or even larger than the critical one, depending on the choice of the edge parameters.

As a result, predictive simulations were required to study pellet injection as an alternative fuelling method. In particular, in accordance with previous studies, we explored the possibility of fuelling the plasma using pellets of three different sizes and velocities (1: r=0.7mm, v=617m/s; 2: r=1mm, v=516m/s; 3: r=1.3mm, v=640m/s), evaluating the optimal injection frequency and the respect of the limits imposed on the post-injection density increase. The results obtained shows that pellets of small size ($r \leq 1$mm) are an excellent alternative to gas puff, as they are able to sustain the desired density levels without causing excessive disturbances and with optimized frequencies well in line with the available injector capacities.

Introduction

In the context of an exponential growth in energy demand, research and optimization of renewable energy sources is of primary importance to minimize our impact on the environment. For this purpose, in the last few decades the scientific community has made many efforts to find proper alternatives to fossil fuels, such as solar power and wind power. Although these two sources are indeed unlimited, the lack of efficient storage systems and the low energy density have made it necessary to study other methods to produce energy in a sustainable way.
One of the most relevant solutions is the controlled thermonuclear fusion, whose physics aspects are presented in chapter 1.

Because of the high temperatures required to promote fusion reactions, Tritium (T) and Deuterium (D) used as nuclear fuel are in the plasma state, which is an ionized gas composed primarily of electrons and positive ions and in which collective particle interactions dominate.
Given the extreme conditions, the plasma is confined by using intense magnetic fields in properly designed configurations. One of the main devices capable of magnetically confining the plasma is the tokamak, which, thanks to its excellent physics performance, is the leading candidate to become the world's first fusion power plant.

There are currently several research centres studying the physics and engineering aspects of such devices. One of these is the Divertor Tokamak Test facility (DTT) [1, 2], which is an experimental reactor under construction at Frascati (Roma), and designed to complete one of the main missions presented in 2012 by the European Roadmap.
The main purpose of the DTT project is to study the controlled exhaust of energy and particles by conveying them to a particular structure called divertor, whose optimal configurations are needed in the pilot reactor DEMO (Demonstration Fusion Power Plant). In chapter 2 the main aspects of tokamaks and the DTT project are discussed.

In order to obtain and maintain good plasma performance, a certain value of the triple product of temperature, density, and energy confinement time must be achieved. These physical quantities strongly depend on turbulent transport mechanisms, which are responsible for particle and heat fluxes from the plasma core to the edge. In this context, it is therefore necessary to balance these continuous losses with auxiliary systems providing the plasma with both energy and particles.
The aim of this thesis work is to investigate for the first time in DTT the main particle fuelling methods, which are gas puff and pellet injection. Furthermore, since DTT is not meant to produce power and hence will not operate fusion between D and T, the supply of particles from outside will involve only the first isotope. The transport and particle sources are discussed in detail in chapter 3.

In order to study and optimize the two fuelling systems for DTT, predictive simulations concerning both particle sources and the plasma response to them are required. Since the plasma behaviour in a tokamak is continuously influenced by nonlinear interactions between different physical processes, it was necessary to include this work in the broader scenario of integrated modelling concerning all the tokamak aspects. This thesis is therefore addressing the DTT fuelling within the framework of integrated modelling of DTT scenarios.
Consequently, to simulate simultaneously the different regions of the tokamak, the simulations presented in this thesis work are carried out within the suite of codes JINTRAC, with the 1.5D transport code JETTO equipped with turbulent transport models Qualikiz and Qualikiz Neural Network. The main aspects of JINTRAC and JETTO are presented in Chapter 4, as well as a summary on the integrated modelling work done so far by the DTT team.
Finally, in chapter 5, my work is fully presented. The first part consists of a series of predictive simulations establishing the nominal level of gas puff which has to be applied to sustain the desired plasma density. This procedure is needed to evaluate if this value exceeds the feasibility limits of the pumping system and the levels beyond which plasma edge degradation would occur.
In the second part, we study pellet injection as an alternative fuelling method. In particular, in accordance with previous studies, we explored the possibility of fuelling the plasma using pellets of three different sizes and velocities, evaluating the optimal injection frequency and the respect of the limits imposed on the post-injection density increase.
A feedback scheme has been implemented for both fuelling methods in order to evaluate the

optimal injection parameters (nominal rate in the first case and frequency in the second one), which are necessary to sustain the density levels required in order to achieve the desired confinement performance.

Chapter 1

Nuclear fusion power

1.1 Binding energy

A nucleus is a system composed of elementary particles that interact through attractive nuclear forces. Exact measurements of atomic weights have shown that the weight of a nucleus is smaller than the sum of the weights of its constituents by a few percent. The mass M_{nucl} is given by

$$M_{nucl} = Z M_p + (A - Z) M_n - \Delta$$

where M_p and M_n are respectively the proton and neutron masses and Δ is the mass defect. The latter is the most evident proof of the famous Einstein mass-energy relation. Knowing that

$$E_{tot,nucl} = M_{nucl} c^2$$
$$E_{s.c.} = [Z M_p + (A - Z) M_n] c^2$$

and operating the difference between the two energies, one can easily derive the work necessary to split out the nucleus into its elementary constituents, the binding energy B, that can be expressed as

$$B = \Delta c^2$$

It is clear that if a nuclear reaction leads to an increase of B, the process is energetically convenient because the resulting product becomes more stable, that is, more work is needed to break the nucleus into its constituents.

It is appropriate to introduce the binding energy per nucleon f (see Figure 1.1), defined as the binding energy divided by the atomic mass number. For atoms with $A \leq 56$ (Iron), f grows with A. In this context, if two light nuclei fuse in a nucleus with $A \leq 56$, the reaction is exothermic.

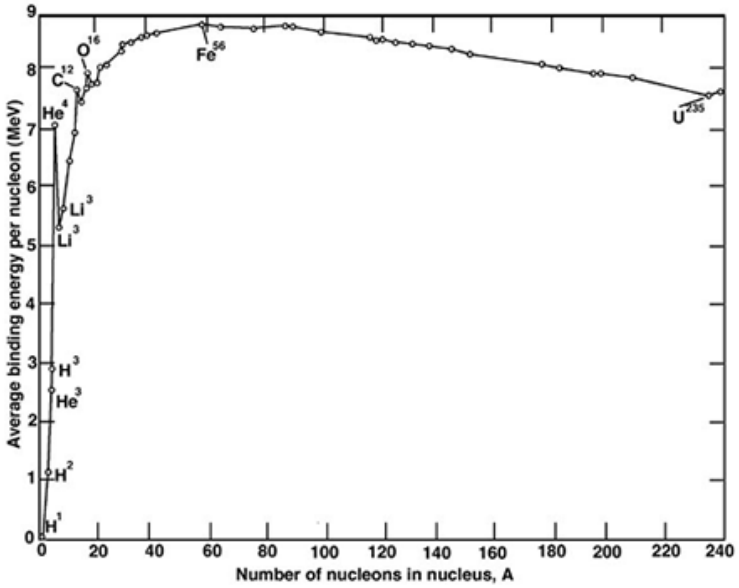

Figure 1.1: Experimental binding energy per nucleon

1.2 Reaction Rate and Cross Section

Generally, a nuclear reaction can be schematized as follows:

$$A + B \rightarrow C + D$$

where $A + B$ represents the *input channel* and $C + D$ the *output channel*.

In the most general view, the reaction rate R is the number of counts of elements of the output channel per unit of time. It can be written as [3]:

$$R_{AB} = n_A n_B < \sigma v >$$

where n_A, n_B are the density of the species A and B, $v = v_A - v_B$ is the relative velocity, and σ is the cross section, that represents the probability of occurrence of a nuclear reaction. In other words, it quantifies the probability that the particle state is changed following the interaction.

Although the physical meaning of the cross section is simple, its functional dependence on v and geometry can not be considered obvious. Tipically, the values of σ for fusion reactions are calculated experimentally by colliding a mono-energetic beam whit a stationary target.

The experimental cross sections are plotted in figure 1.2 for the three main fusion reactions (see Paragraph 1.3).

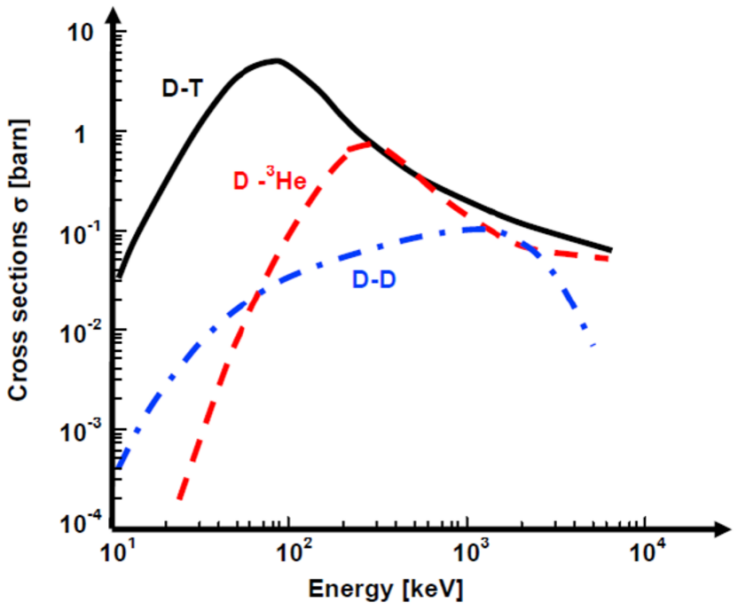

Figure 1.2: Experimental cross section for the $D-T$, $D-He^3$, and $D-D$ fusion reactions as a function of deuterium kinetic energy K_D.

Thus, assuming the σ trend as known and exploiting the Maxwellian distribution function, the *reactivity* $<\sigma v>$ can be numerically found (see Figure 1.3). Observe that the D-T reaction presents a maximum of about $10^{-21}\, m^3/s$ at T around 100 keV, while both $D-D$ and $D-He^3$ trends show a less peaked profile. This will be a crucial point in the next paragraph, where advantages and disadvantages of different reactions between light elements will be discussed.

1.3 Light elements fusion reaction

Mainly, three fusion reactions between light nuclei are advantageous for the production of nuclear energy [3]. These require deuterium, tritium and helium-3, an isotope of helium.

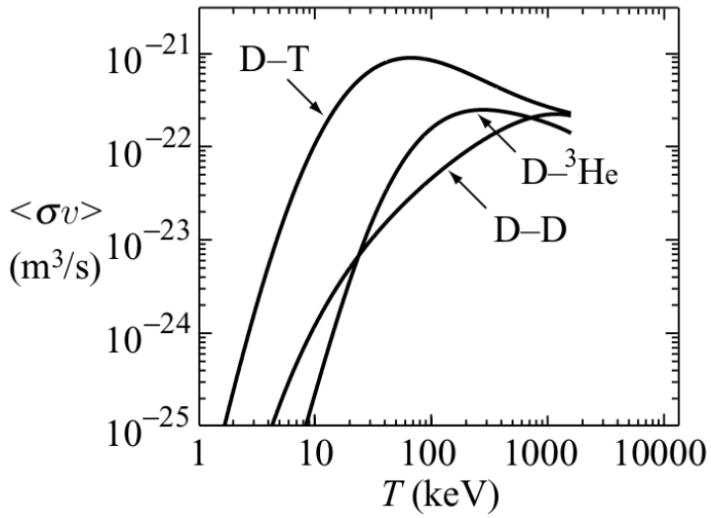

Figure 1.3: Numerical reactivity for the $D-T$, $D-He^3$, and $D-D$ fusion reactions as a function of temperature.

The D-D reaction

The D-D reaction is the fusion between two deuterium nuclei. It has two relevant branches as follows:

$$D+D \rightarrow He^3+n+3.27\ MeV$$

$$D+D \rightarrow T+p+4.03\ MeV$$

Although it is apparently the most convenient choice since the deuterium is easily accessible from the ocean, this reaction is difficult to initiate because of the lower cross section at higher temperatures.

The D-He^3 reaction

This reaction consists of fusing a deuterium nucleus with one of helium-3 as follows:

$$D+He^3 \rightarrow \alpha+p+18.3\ MeV$$

The large amount of energy released and the fact that no neutrons are produced seems to make this reaction desirable. However, the low He^3 availability combined with the difficulty of initiating $D-He^3$ fusion (see Figure 1.3) are the reasons that current fusion research is not focused on this reaction.

The D-T reaction

The D-T reaction is the fusion between a deuterium nucleus and a tritium nucleus. It can be written as

$$D + T \rightarrow \alpha + n + 17.6\ MeV$$

Although the tritium is not present naturally on earth, the advantages overcome the limited availability of the isotope. Indeed, this reaction produces a significant amount of energy and it is the easiest to obtain due to its higher cross section at lower temperatures. For these reasons, the D-T reaction is the one chosen for the realization of the controlled thermonuclear fusion.

A further point of interest concerns the fact that the temperatures needed to initiate fusion reactions are about tens of keV, that means millions of °C. This typically overcomes the ionization potential, thus the D-T mixture is necessarily a fully ionized gas called plasma.

1.4 Plasma and confinement

A *plasma* [4] is an ionized gas composed principally of electrons and positive ions. Since any gas always presents a certain degree of ionization, not every ionized gas could be called a plasma, but only those gases characterized by *quasi-neutrality* and that exhibit a *collective behaviour* between particles.

The quasi-neutrality derives from the concept of *Debye shielding*, that expresses the capability of the plasma to shield the potential of any charged particle thanks to the formation of a surrounding cloud composed of opposite charged particles. In fact, the plasma is usually quasi-neutral because typical plasma particles do not have enough thermal energy to escape from this ”shielding cloud”.

As pointed out in 1.2, in order to initiate fusion reactions, the required temperatures inside the plasma are about tens of keV. Thus, in the realisation of any nuclear fusion device, a crucial necessity is separating the plasma from the machine wall. Moreover, in order to achieve good fusion performance, the value of the triple product of plasma temperature, density, and energy confinement time (see 1.5) must be higher than a critical threshold (*Lawson criterion*), making it necessary to find a confinement technique as efficient as possible.

Nowadays, due to the better results obtained, the *magnetic confinement* (see chapter 2) is the most exploited method to confine a fusion plasma.

1.5 Power balance in a fusion reactor

At this point, it is clear that high temperatures are required to achieve favorable conditions for the D-T fusion reaction. Thus, power losses due to irradiation, Coulomb collisions, and turbulence must be compensated by exploiting auxiliary heating power systems. This considerations lead to a simple form of the steady state power balance relation in a fusion reactor [3]

$$S_\alpha + S_h = S_B + S_k \tag{1.1}$$

where S_α is the fusion power due to alpha particles, S_h represents the input heating power, while S_B and S_k are respectively the power losses driven by Bremsstrahlung radiation and thermal conductivity. The latter is typically higher than the one calculated in the classic theory concerning just Coulomb collisions since the plasma is interested by micro-turbulence that lead to a consistently increase in transport coefficients. The losses due to thermal conductivity can be expressed using the energy confinement time τ_E, given by

$$\tau_E = \frac{W}{P_L}$$

where W is the total plasma energy and P_L the non-irradiated energy loss rate. τ_E represents the relaxation time of the plasma energy due to heat conduction.

The general equation (1.1) can be adapted to three different operating regimes of a fusion reactor:

- **Ideal ignition** characterized by negligible heat conduction losses ($\tau_E \to \infty$) and no auxiliary heating. The balance (1.1) becomes:

$$S_\alpha = S_B$$

- **Ignition**, a more realistic situation in which the alpha heating is high enough to compensate both Bremmstrahlung and conduction losses:

$$S_\alpha = S_B + S_k$$

- **Power amplification** where the external heating is required ($S_h \neq 0$).

Although the first two regimes are more attractive, in cases in which the alpha particle power is not sufficiently large to balance the losses, the amplification regime is still a reasonable way to run the reactor, at least as long there is a net gain in output thermal power.

1.6 The power gain factor Q

The power gain factor Q is defined as [3]:

$$\begin{aligned} Q &= \frac{total\,thermal\,power\,out - heating\,power\,in}{heating\,power\,in} \\ &= \frac{P_{out} - P_{in}}{P_{in}} \end{aligned}$$

In a nuclear fusion reactor, as in any power plant, the ultimate purpose is to convert thermal power into electricity. Thus, it is of primary importance a net gain in the output thermal power, and so the definition of the gain factor Q and its evaluation is crucial.

The most attractive regime for a steady state operation is given by $0 < Q < \infty$. Indeed, $Q = 0$ is the lower limit scenario in which $P_{out} = P_{in}$ and no fusion reactions take place. On the other hand, $Q = \infty$ describes the upper limit of operation: the ideal ignition.

Nevertheless, even if Q provides a useful accounting of the gain of the fusion processes, it does not involve the net electrical output. Thus, in order to have an overview of the power fluxes inside the reactor (see figure 1.4), another parameter is still required, the engineering gain factor Q_E, given by [3]:

$$\begin{aligned} Q_E &= \frac{total\,electric\,power\,out - electric\,power\,in}{electric\,power\,in} \\ &= \frac{P_{out,E} - P_{in,E}}{P_{in,E}} \end{aligned}$$

$P_{in,E}$ is the input electric source needed to supply the auxiliary heating system. It can be easily related to the input thermal power *Pin* as follows:

$$P_{in,E} = \frac{P_{in}}{\eta_e\,\eta_a}$$

where η_e is the efficiency associated with the conversion from an electric source into a power exploitable from the plasma, and η_a describes the fact that the plasma could not absorb the entire input thermal power. Typically, $\eta_e \approx 0.7$ and $\eta_a \approx 0.7$.

By way of example, the DEMO major system block diagram is reported, including the schematic view of power flow in the reactor.

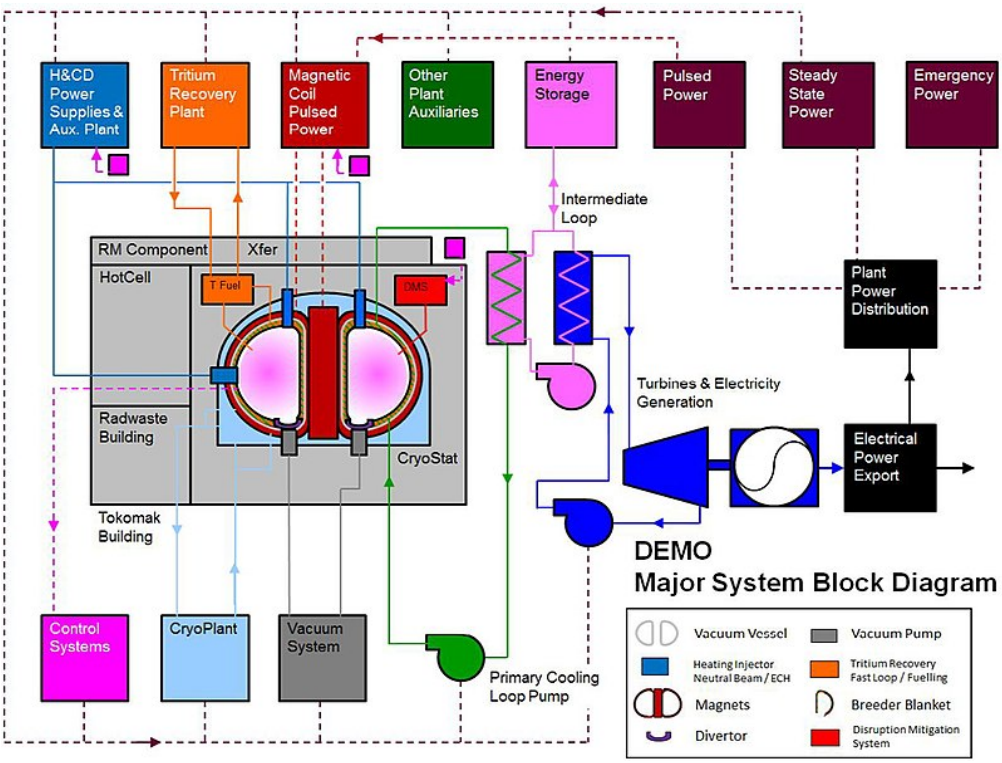

Figure 1.4: DEMO major system block diagram

Chapter 2

The tokamak configuration and the Divertor Tokamak Test facility

2.1 Tokamak generalities

In order to discuss the Divertor Tokamak Test facility (DTT), we need to introduce some fundamental concepts about plasma confinement and tokamaks in general. Indeed, the aim of this section is to investigate issues regarding plasma equilibrium and stability, important parameters and standard modes of operation. To proceed, the first step is to introduce the concepts of plasma equilibrium.

2.1.1 Plasma equilibrium and the tokamak configuration

As previously discussed, in order to confine particles in an efficient way, the magnetic confinement is always required in a fusion reactor. Then, learning how magnetic field lines can hold a plasma in conditions of equilibrium and macroscopic stability becomes a crucial issue. All those studies are based on a single-fluid model known as Magnetohydrodynamics (MHD) [4], whose structure is composed by a closed set of equations as follows:

$$\frac{d\rho}{dt} = \rho \nabla \cdot \mathbf{v} \tag{2.1}$$

$$\rho \frac{d\mathbf{v}}{dt} = \mathbf{J} \times \mathbf{B} - \nabla p \tag{2.2}$$

$$\frac{d}{dt}\left(\frac{p}{p^{\gamma}}\right) = 0 \tag{2.3}$$

$$\mathbf{E} + \mathbf{v} \times \mathbf{B} = \eta_{||}\mathbf{J} \tag{2.4}$$

$$\nabla \times \mathbf{E} = -\frac{\partial \mathbf{B}}{\partial t} \tag{2.5}$$

$$\nabla \times \mathbf{B} = \mu_0 \mathbf{J} \tag{2.6}$$

$$\nabla \cdot \mathbf{B} = 0 \tag{2.7}$$

$$\nabla \cdot \mathbf{E} = \frac{\rho}{\varepsilon_0} \tag{2.8}$$

The equations represent respectively the conservation of mass, momentum, and energy, the Ohm's law in a resistive plasma, and the Maxwell's laws. This closed set allows to study the magnetic configurations needed to confine the plasma.

The static equilibrium is derived by two assumptions:

- All physical quantities are time independent $\left(\frac{\partial}{\partial t} = 0\right)$
- The plasma velocity $\mathbf{v} = 0$

In this context, the equation (2.2) becomes the balance between the magnetic force $\mathbf{J} \times \mathbf{B}$ and the plasma pressure force ∇p as follows:

$$\mathbf{J} \times \mathbf{B} = \nabla p \tag{2.9}$$

The equations (2.6), (2.7) and (2.9) define the MHD equilibrium model. If one combines the latter with a magnetic toroidal geometry, it is possible to derive the Grad-Shafranov equation, given by:

$$\Delta^* \psi = -\mu_0 r^2 \frac{\partial p}{\partial \psi} - F(\psi)\frac{\partial F}{\partial \psi}$$

where μ_0 is the *magnetic permeability*, ψ the magnetic flux function, p the pressure, and $F(\psi) = rB_\theta$, with B_θ the poloidal magnetic field. The Grad-Shafranov equation expresses the equilibrium of a toroidal magnetic configuration.

One device that reflects this particular field geometry is the tokamak, an axisymmetric torus become the leading candidate to be the world's first fusion reactor. The tokamak has a large toroidal magnetic field B_T, produced by toroidal field coils, and a moderate toroidal plasma current I_T. The

latter is driven inductively using an ohmic transformer in which coils are the primary circuit, and the plasma is the secondary. The plasma current is required for two reasons: ohmic heating and equilibrium. Indeed, I_T induces a poloidal magnetic field B_P needed to confine particle orbits inside the plasma. Additionally, an external vertical magnetic field is applied to guarantee the correct plasma positioning. Thus, the resulting total field presents helical field lines as shown in figure 2.1.

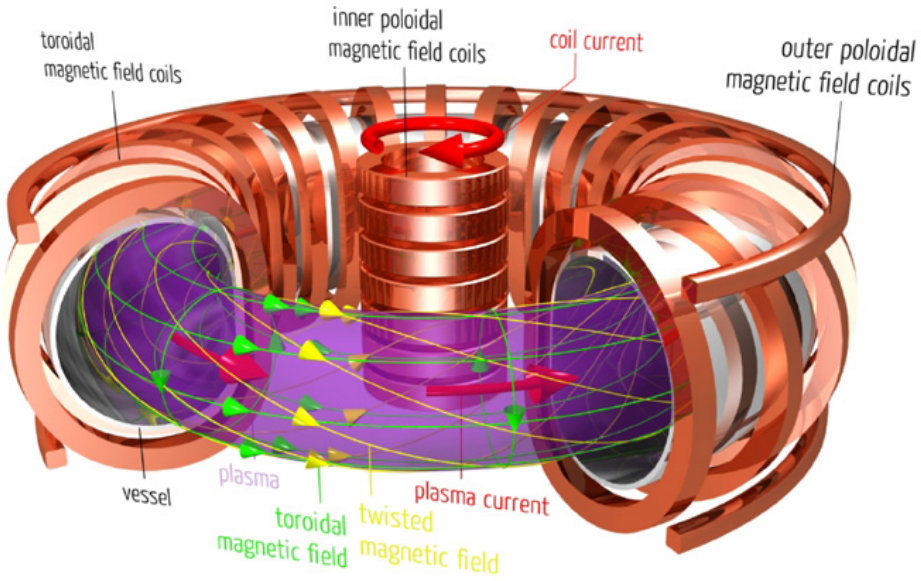

Figure 2.1: Tokamak magnetic twisted field lines that cover the magnetic surface

The particles follow these twisted field lines performing a rotation motion around them. The flux surfaces on which the helical field lines lie are iso-p surfaces and act as barriers which can be crossed just during transversal drifts or collisions.

In plasma physics, β is a fundamental parameter when the confinement efficiency is treated [5]. It is given by:

$$\beta = \frac{p}{B^2/8\pi}$$

and it expresses the ratio between kinetic and magnetic pressure. Since this quantity is related to ideal MHD instabilities, many numerical studies were made to determine the highest possible stable β for various geometries and profiles. One of them has produced a very simple empirical relation for the optimized β limit:

$$\beta \leq \beta_{crit} \equiv \beta_N \frac{I}{aB_0}$$

where β_N is a numerical coefficient. For $\beta_N = 2.8$ this limit is called the *Troyon Limit*. The value of β_{crit} is also related to the poloidal shape. Indeed, one way to improve the β limit is to force the plasma to have a non-circular cross section in order to obtain an elongated, triangular one. For this reason, although first devices were designed with a circular section, in recent years most of reactors are characterized by a D-shape (see figure 2.2).

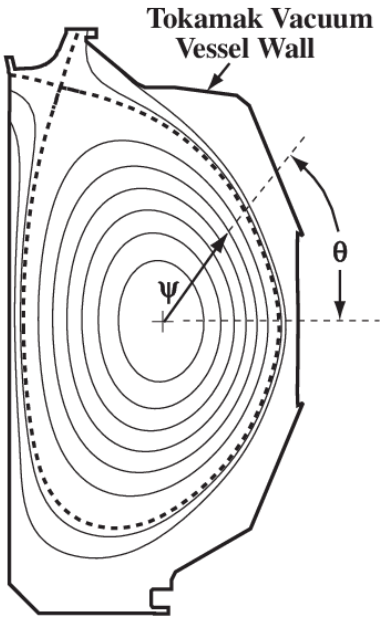

Figure 2.2: Tokamak poloidal cross section with a D-shape

Another important parameter is the *safety factor* q, given by:

$$q = \frac{d\,\Phi_T}{d\,\psi_P} \approx \frac{1}{2\,\pi} \int \frac{r}{R} \frac{B_T}{B_P}\, d\theta$$

where Φ_T and ψ_P are the toroidal and poloidal magnetic fluxes, while r and R are respectively the minor and major radius.

In case q is expressible as a ratio of two integers, ($q = \frac{m}{n}$ i.e. q is rational), the magnetic field force line returns on itself after m toroidal turns and n poloidal turns, so it does not ergotically cover the magnetic surface. In this context, it can be shown that a perturbation characterized by the same waves number m and n could be unstable [4]. Nevertheless, if the radial derivative of the safety factor, the *magnetic shear*, is high enough, the stability is still guaranteed. Thus, the safety factor q plays a crucial role in plasma stability.

2.1.2 Standard mode of operation

When the auxiliary heating is applied to a plasma, it usually begins in a mode of operation with a relatively low energy confinement time τ_E, known as the L-mode. If the external input power increases, the plasma will undergo a transition to a higher confinement mode of operation, known as H-mode. The interest in running the reactor in this way is the enhancement of the confinement performance due to the presence of an *Edge Transport Barrier* (ETB), also known as *Pedestal* (an example in Figure 2.3). The latter is an external region of the plasma core in which turbulent transport is reduced by sheared flows in the poloidal direction. For these reasons, the H-mode is nowadays the principal mode of operation under investigation in the DTT facility.

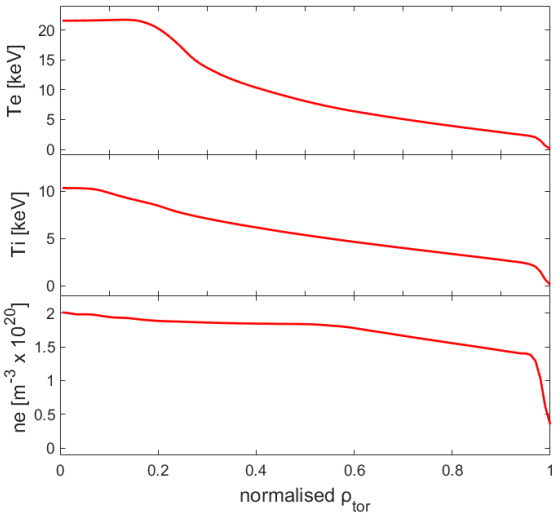

Figure 2.3: Temperature and density profiles characterized by an Edge Transport Barrier.

2.1.3 The particle exhaust and the divertor

As previously discussed, in order to reach and maintain high temperatures, the plasma needs to be heated by external systems and alpha particles. The resulting input power can be expelled via charged particles, neutral particles, or radiation. In the last two cases, magnetic surfaces do not operate as barriers since photons and neutral particles do not follow magnetic field lines, and so the power released interests a large area.

On the contrary, charged particles are strongly influenced by the magnetic configuration; indeed, they follow the twisted magnetic lines and are conveyed to a relatively small portion of the wall.

Consequently, the power exhaust due to charged particles can lead to strong thermal stresses since structural materials are interested by higher power densities.

The general idea is to control this particle exhaust using a divertor, a component made of a material part and a non-material one. Its operating principle is based on a particular magnetic configuration called *X-point* (see Figure 2.4), whose presence heavily modifies the particle transport in the SOL (scrape off layer), the region outside the separatrix. The resulting trajectories impose that the particles are conveyed to the divertor plates meant to withstand thermal loads up to $10\,\frac{MW}{m^2}$.

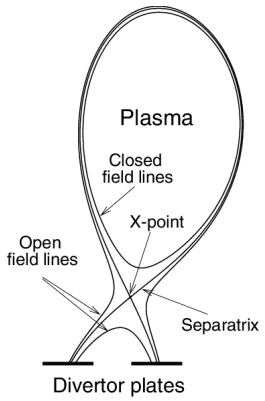

Figure 2.4: Schematic view of a divertor configuration

2.2 The DTT project

The Divertor Tokamak Test Facility (DTT), under construction in Frascati, Italy, is an experimental fusion reactor meant to pursue one of the principal missions presented in 2012 by the European Roadmap to the realization of the fusion energy. Its purpose is to support the main project DEMO (*Demonstration Fusion Power Plant*) exploring various solutions concerning an efficient heat and particle exhaust system.

Indeed, it is clear that alternative divertor solutions must be tested in a DEMO-relevant environment, that is in a machine with DEMO relevant values of P_{sep}/R (where P_{sep} is the power crossing the separatrix) and at the same time a reactor-grade plasma core, which is not achieved by present devices. To cover this gap, the DTT machine has been design. Thus, DTT will have high magnetic field, high input power (up to 45 MW) and a relatively small major radius. The main goal of DTT is to test various divertor solutions in a DEMO relevant regime.

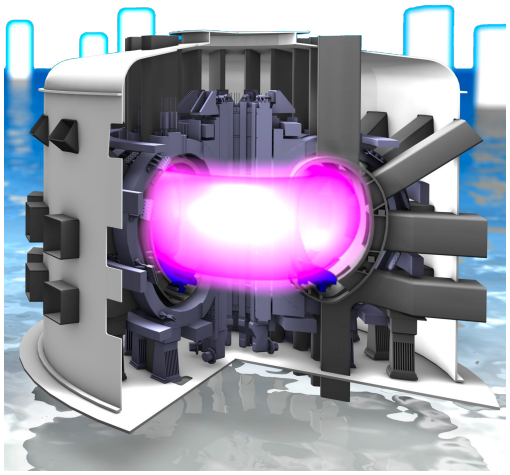

Figure 2.5: Sectional view of DTT. From DTT IDR 2019 WEB.

Although the main physical and technological characteristics were defined in 2017, the scientific team has continued to update the project. The newest machine setup is defined by the following main parameters:

	DTT	**DEMO**
R (m)	2.19	9.1
r (m)	0.70	2.93
A	3.1	3.1
I_p (MA)	5.5	19.6
B (T)	5.85	5.7
P_{tot} (MW)	45	460
P_{sep}/R (MW/m)	15	17
λ_q (mm)	0.7	1.0
Pulse Length (s)	100	7600
κ	≤ 1.89	1.65-1.75
δ	≤ 0.4	≈ 0.3

Table 2.1

where **R** and **r** are the major and minor radius, **A** is the *Aspect Ratio*, I_p and **B** are the plasma current and the magnetic field, λ_q is the power decay length in the SOL region, κ the elongation, and δ the average triangularity.

2.2.1 Plasma Heating

In order to run the DTT reactor in a DEMO-relevant environment a ratio $P_{sep}/R \approx 15$ MW/m is required. It can be obtained thanks to an external input power of 45 MW produced by a mix of auxiliary heating systems: Electron Cyclotron Resonance Heating (ECRH), Ion Cyclotron Resonance Heating (ICRH) and Neutral Beam Injection (NBI) [3].

Electron and Ion Cyclotron Resonance Heating

A charged particle in a magnetic field **B**, with a non-zero velocity in the direction perpendicular to **B**, moves in a circular motion around the magnetic field lines whit a radius ρ_L (*Larmor radius*) and an angular frequency (*Cyclotron frequency*) given by:

$$\omega = \frac{qB}{m}$$

where q and m are the particle's charge and mass. If an electromagnetic wave is launched into the plasma with an angular frequency ω_{rf}, the particles with $\omega_j = \omega_{rf}$ can absorb energy from the wave by resonant effects. In this context, Electron and Ion CRH systems are based on using a radio-frequency antenna that generates waves with frequency equal to the cyclotron of electrons and ions.

Neutral Beam Injection NBI

The Neutral Beam Injection consists in an acceleration line that injects highly energetic neutral atoms inside the tokamak. Once the beam particles enter the plasma edge they collide with electrons and ions and are ionized. The resulting charged particles are captured by the magnetic field and start to transfer energy to the plasma through Coulomb collisions with thermal ions and electrons. Thus, the NBI is a source of both heat and particles. The NBI heating efficiency is strongly influenced by the penetration capability of the beam inside the plasma core.
The interaction between neutral atoms and plasma particles consists in three events:

- **Charge exchange**: $A_{beam} + A^+_{plasma} \rightarrow A^+_{beam} + A_{plasma}$
- **Ionization with ions**: $A_{beam} + A^+_{plasma} \rightarrow A^+_{beam} + A^+_{plasma} + e^-$

- **Ionization with electrons**: $A_{beam} + e^- \rightarrow A^+_{beam} + 2e^-$

Knowing that σ_{cx}, σ_e and σ_I are the cross sections for this interactions, and that the intensity of the injected beam is given by:

$$I_b = N_b \, v_b$$

it is possible to derive the intensity decay as follows:

$$\frac{d\,I_b}{d\,x} = -n \left(\sigma_{cx} + \sigma_I + \frac{< \sigma_e \, v_e >}{v_b} \right) \tag{2.10}$$

where v_b is the beam velocity, $n = n(x)$ the plasma particle density, N_b the beam particle number, and v_e the electron velocity.
As expected, the equation (2.9) shows opposite signs between the intensity decay in space and cross sections, that is, a bigger reaction rate leads to a decrease in the penetration capability.

DTT heating program

The 45 MW of total heating power are not meant to be immediately available to the tokamak. At the so called day-1 (during the day-0 only internal ohmic heating and 8 MW from ECRH are provided) the input power will be such as to achieve the H-mode operation in a 4 MA plasma. This will require $\sim$ 23 MW progressively injected in the system. Indeed, the first experimental plasma (magnetic field 3T, plasma current up to 2 MA) is compatible with 8 MW of ECRH, while for the injection of the rest of the power the magnetic field will be increased up to the 6 T nominal value, with a plasma current of 4 MA. The day-1 additional power configuration will be composed by 1 NBI injector supplying 7.5 MW to the plasma, 2 ICRH antennas (1.5 MW from each antenna) and 16 MW installed from 16 gyrotrons at 170 GHz. During this first injection phase, the design of the final stage (45 MW) will be finalized and completed. This strategy will reduce the risk in the procurement of the DTT power systems, leaving enough time to verify, evaluate and modify the initial design.

2.2.2 DTT Diagnostics

In the DTT project the diagnostics are essential for safety, feedback control of plasma parameters and to evaluate in detail the core performance and power and particles exhaust channel [2]. Thus,

the pedestal and the divertor will be specially observed, as well as the quality of the confinement and the divertor efficiency. Obviously, the systems used have to not perturb the plasma to get truthful measurements and also must be designed to withstand extreme conditions inside the vessel.

Since most of mid-plane ports will be occupied by auxiliary heating systems, diagnostic instruments could share the location with other components such as cooling tubes or electricity grids.
In this paragraph, some of the main DTT diagnostics are briefly discussed.

Magnetic probes

Magnetic probes have the purpose to measure the plasma current and its radial and vertical position. Preliminary analysis underline that this result can be obtain with less than 1% error locating the probes in six different poloidal positions both inside and outside the vacuum vessel.
These probes consists in biaxial coils whose wires are made of different coating materials in relation of the position of the probe since inner and outer coils need to withstand different thermal stresses.

Plasma equilibrium and shape

In addition to the standard magnetic measurements, DTT will be equipped with a diagnostic system capable of evaluating the plasma equilibrium and shape. A technique used for this purpose is based on two interferometer-polarimeter systems composed by a few mid infrared (MIR) channels (10 μm), a CO2/CO toroidal system (5 μm) and a higher spatial resolution poloidal far infrared (FIR) one.
This diagnostic is able to measure the plasma current and density profile, and the chord average electron density. Thanks to its high number of channels distributed in the tokamak, this method will have enough resolution for a good equilibrium reconstruction.

Core electron density profile

The main diagnostic technique used to evaluate the electron density profile n_e is the *High Resolution Thomson Scattering* (HRTS).
A laser is launched into the plasma core where it interacts with the electrons via Thomson scattering. Thus, the scattered photons have the same energy, and so the same frequency, of the incident photons since the scattering is elastic. Once those emitted photons are properly collected, it is

possible to measure the intensity of the scattered beam. The latter is proportional to the scattered photon number and so to the electron number, that allows to evaluate the electron density.
In DTT the laser source is a Nd:YAG (λ = 1064 nm), the scattering volumes are defined using fibre optics and the emitted laser light is measured exploiting a silicon avalanche photo diode detector.
There are two possible geometries: in the first one the laser beam crosses vertically the plasma with entrance and exit on an upper and lower port. In the second configuration the laser beam enters in the vacuum vessel from an equatorial port and, after crossing the plasma horizontally, it is collected by the detector. This technique allows to achieve a spatial resolution of 3 cm in a range $n_e > 10^{19}\ m^{-3}$.

Divertor diagnostics

In line with the main objective of the DTT project, various diagnostic techniques are dedicated to explore plasma parameters in the divertor region. In particular, they are focused on evaluating the impurity level, the divertor strike points position and heat loads, plasma detachment, degree of enrichment of impurities and level of helium compression.
Once again, in order to characterize the edge and divertor region, it is possible to take advantage of the Thomson scattering (TS) to measure T_e and n_e. The adopted diagnostic system is the same described for the core kinetic profiles. Indeed, a conventional TS based on a Nd:YAG laser and a set of fibre optics is considered.
Nevertheless, the system geometry is slightly different from the one discussed in the previous paragraph, since in this layout the laser enters the divertor from the lower-outboard side (see Figure 2.6) passing through the aperture between two adjacent divertor cassettes and is dumped on the inner side of the first wall.
Another useful technique used to characterize the divertor region is the *Divertor Spectroscopy*. Its aim is to determine plasma position and kinetics of impurities and main gas (once again using the broadening due to the Doppler effect).
Although spectroscopy in the mid-plane region requires a range from visible to soft X-ray, here in the divertor the spectrum has to be enlarged up to 125 nm to monitor the main emitting species including molecules.

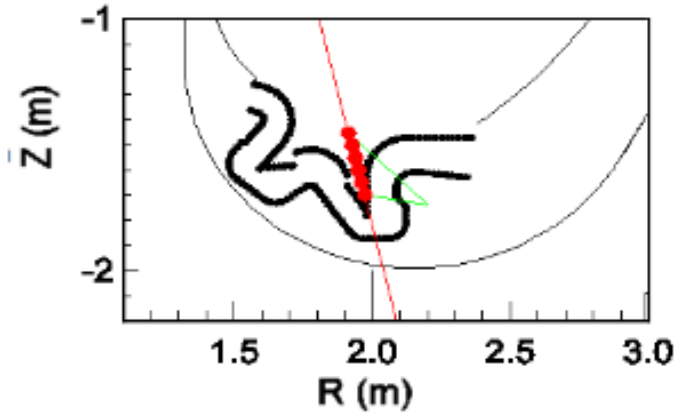

Figure 2.6: Divertor TS layout.

Turbulence diagnostics

Various techniques are available to study the fluctuation properties of both core and edge turbulence transport, investigating phenomena like Edge Localized modes (ELMs), Alfven modes, zonal flows, Ion Temperature Gradient instabilities (ITG), and Trapped Electron modes (TEM). In this context, optical diagnostics such as Gas Puffing Imaging and Thermal Helium beams can be used to study and characterize density and temperature fluctuations. These systems should be positioned both on the mid-plane region and in divertor proximity.
By way of example, it is possible to study the ELMs dynamic using an Electron Cyclotron Emission Imaging (ECEI), while to evaluate the fluctuation level of density and temperature in the core other techniques like Beam Emission Spectroscopy and Correlation Doppler Reflectometry are exploited.

2.2.3 The DTT operational program

The DTT project is meant to last a considerable period of time (25 years). It will be divided into different phases, each with different purposes. The first operational phase will be dedicated to the realization and installation of the various components of the machine. Then, the aim will be reaching a robust H-mode of operation to guarantee a DEMO-relevant environment in which various divertor and new magnetic configurations will be tested.

As previously discussed, the total auxiliary power are not meant to be immediately injected inside the tokamak, but will be gradually increased in the system depending on the operational program (see Figure 2.8).

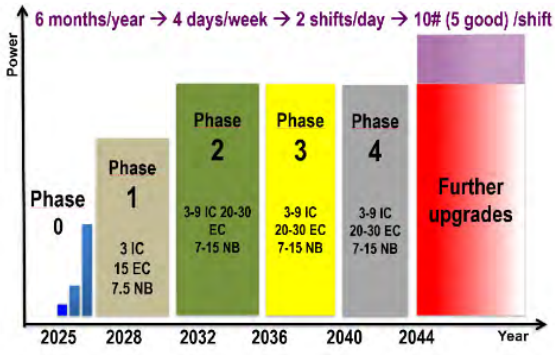

Figure 2.7: The DTT scientific program through the years

Chapter 3

Transport and fuelling

During its operation, the tokamak is constantly interested by particle losses induced by turbulent transport mechanisms that occur in a plasma. This leads to a decrease in plasma densities, and hence in plasma confinement and performances (the fusion reaction rate R is proportional to the product between densities $n_1 n_2$, see chapter 1).
Clearly, this creates the need to refuel the plasma with an external particle injection, in order to keep the density levels constant.
This thesis work has the purpose to investigate for the first time the deuterium fuelling in the DTT plasma, dealing in particular with the study of the plasma response to particle sources.
Since the plasma density levels and the interaction between plasma and particle sources strongly depends on turbulent transport mechanisms, a section dedicated to illustrate the physical aspects of transport theory is needed.
After that, the main particle sources exploited to fuel the DTT plasma are examined in detail.

3.1 Transport equations

Consider a set of particles of a certain species moving in the phase space. The particle number N in a volume V contained in the phase space, is given by:

$$N = \int_V f(\vec{x}, \vec{v}, t) d^3\vec{x} d^3\vec{v}$$

where $\vec{x}$ is the position, $\vec{v}$ the velocity, and $f(\vec{x},\vec{v},t)$ the particle distribution function.

In the absence of particle sources and sinks, the number N is conserved:

$$\frac{dN}{dt} = 0 \Longrightarrow \frac{\partial N}{\partial t} + \Gamma_S(N) = 0 \tag{3.1}$$

where Γ_S is defined as:

$$\int_S f(\vec{x},\vec{v},t)\vec{V} \cdot d^5\vec{S} \tag{3.2}$$

with $\vec{V}$ the velocity in the phase space. The expression (3.2) represents the particle net flux through the surface S that encloses V.

Exploiting the divergence theorem and neglecting collisions, the equation (3.1) can be rewritten as:

$$\frac{\partial f}{\partial t} + \vec{v} \cdot \frac{\partial f}{\partial \vec{x}} + \frac{\vec{F}}{m} \cdot \frac{\partial f}{\partial \vec{v}} = 0 \tag{3.3}$$

where $\vec{F}$ is the force acting on the particle and m is the particle mass. The (3.3) is called *Boltzmann* equation, and describes the evolution of the particle distribution function $f(\vec{x},\vec{v},t)$ in the phase space, assuming no frictions and a lack of sources and sinks.

In the specific case of plasma within tokamaks, a particle with charge q feels the Lorentz force $\vec{F} = q(\vec{E} + \vec{v} \times \vec{B})$, and hence the (3.3) becomes the so-called *Vlasov* equation:

$$\frac{\partial f}{\partial t} + \vec{v} \cdot \frac{\partial f}{\partial \vec{x}} + \frac{q}{m}(\vec{E} + \vec{v} \times \vec{B}) \cdot \frac{\partial f}{\partial \vec{v}} = 0 \tag{3.4}$$

The latter can be rewritten also considering the contribution of collisions and the presence of particle sources, leading to a more comprehensive equation:

$$\frac{\partial f}{\partial t} + \vec{v} \cdot \frac{\partial f}{\partial \vec{x}} + \frac{q}{m}(\vec{E} + \vec{v} \times \vec{B}) \cdot \frac{\partial f}{\partial \vec{v}} = \left(\frac{\partial f}{\partial t}\right)_{coll} + S \tag{3.5}$$

where $\left(\frac{\partial f}{\partial t}\right)_{coll}$ is the collisional term and S the source one.

The former can be described by the *Fokker-Planck* equation [5]:

$$\left(\frac{\partial f}{\partial t}\right)_{coll} = -\frac{\partial}{\partial \vec{v}}\left[f(\vec{v},t)\left\langle\frac{\Delta\vec{v}}{\Delta t}\right\rangle\right] + \frac{1}{2}\frac{\partial}{\partial \vec{v}}\frac{\partial}{\partial \vec{v}} : \left[f(\vec{v},t)\left\langle\frac{\Delta\vec{v}\Delta\vec{v}}{\Delta t}\right\rangle\right]$$

where $f(\vec{v},t)$ is related to the probability that a particle has a velocity v at instant t. Furthermore, $\Delta\vec{v}$ is the change in velocity following a collision and Δt is such that $(t - \Delta t)$ represents the initial time of this change in velocity.

Since $\langle \Delta\vec{v}/\Delta t \rangle$ is the mean acceleration, the first addend represents a friction term due to collisions. On the other hand, the second addend includes the matrix of the velocity mean spreading $\langle \Delta\vec{v}\Delta\vec{v}/\Delta t \rangle$, and hence stands for a diffusive term due to the collisions.

The problem of heat and particle transport is described by a set of equations as follows:

$$\frac{\partial n_{e,i}}{\partial t} + \nabla \cdot \vec{\Gamma}_{e,i} = S_{e,i} \tag{3.6}$$

$$\frac{\partial \left(\frac{3}{2} T_{e,i} n_{e,i} \right)}{\partial t} + \nabla \cdot \left(\vec{q}_{e,i} + \frac{5}{2} T_{e,i} \vec{\Gamma}_{e,i} \right) = Q_{e,i} \tag{3.7}$$

where $n_{e,i}$ is the plasma density (electron and ion, respectively), $T_{e,i}$ is the plasma temperature (again electron and ion), $\vec{q}_{e,i}$ and $\vec{\Gamma}_{e,i}$ are the heat and particle fluxes, while $Q_{e,i}$ and $S_{e,i}$ represent heat and particle sources and sinks.
The (3.6) is the *continuity equation*, while the (3.7) represents the *energy conservation*. They are derived calculating the zeroth and the second moment of the Vlasov equation, respectively.
Furthermore, it is possible to obtain the *momentum equation* from the (3.5) first moment. Nevertheless, it is not directly relevant to the development of this thesis work.

In light of Fourier's studies on heat transport, it is clear that gradients of directly observable thermodynamic variables, such as temperature and density, can be related to the respective heat and particle fluxes. In general, it is possible to write:

$$\vec{F} = -\underline{\underline{D}} \nabla \vec{u} + \underline{\underline{V}} \vec{u} \tag{3.8}$$

where

$$\vec{F} = \begin{pmatrix} \vec{\Gamma}_e \\ \vec{q}_e / n_e \\ \vec{q}_i / n_i \end{pmatrix} \qquad \vec{u} = \begin{pmatrix} n_e \\ T_e \\ T_i \end{pmatrix}$$

while $\underline{\underline{D}}$ and $\underline{\underline{V}}$ are the transport coefficient matrices concerning diffusion and convection, respectively. They are given by:

$$\underline{\underline{D}} = \begin{pmatrix} D_e & c_{12} & c_{13} \\ c_{21} & \chi_e & c_{23} \\ c_{31} & c_{32} & \chi_i \end{pmatrix} \qquad \underline{\underline{V}} = \begin{pmatrix} v_e & a_{12} & a_{13} \\ a_{21} & U_e & a_{23} \\ a_{31} & a_{32} & U_i \end{pmatrix}$$

D_e and v_e represent the electron diffusion and convection coefficients for particles, $\chi_{e,i}$ is the heat diffusion coefficient for electrons and ions respectively, and $U_{e,i}$ is the heat convection coefficient. The extra-diagonal terms represent the coupling between the different thermodynamic variables and account for a possible flow originating from a gradient of a variable not directly associated. Since these coefficients can be functions of plasma parameters and their gradients, the fluxes are non linear functions of the thermodynamic variable gradients.

3.2 Neoclassical transport

Understanding and calculating the transport matrix elements is one of the main goals of transport studies.

The simplest reference model is the *random walk* in which the purpose is to describe how a particle diffuses following a series of N random collisions.

Any particle that follows the magnetic field lines and undergoes a Coulomb collision will be affected by a certain displacement Δx with respect to the line on which it was previously moving. This concept embodies the essence of particle diffusion.

Now, knowing that τ is the characteristic time between two consecutive collisions, one can derive the diffusion coefficient D as:

$$D = \frac{(\Delta x)^2}{\tau}$$

It is possible to apply the random walk model to a plasma with a cylindrical geometry: that description is called classical transport.

However, advanced studies and experiments showed that this simple model is unsuitable for describing what happens in a toroidal plasma. Indeed, the classical transport really underestimates the diffusion coefficient D.

Toroidicity introduces the possibility that the longitudinal and transverse particle motions with respect to the field lines are coupled, leading to a substantial increase in transport coefficients.

Precisely because of a geometry of this type, the tokamak presents a radial magnetic field gradient. This results in a fraction of particles not having enough energy to complete an entire toroidal turn during their revolution, resulting in a trapped motion.

Indeed, when their kinetic energy is to balance the magnetic potential, they reverse their direction,

giving rise to a poloidal orbit reminiscent of the shape of a banana, hence the name banana orbit (see Figure 3.1).

The presence of particles following these particular trajectories heavily influences transport in a tokamak. Indeed, although the Δx of the classical model is of the order of the Larmor radius r_L, in the case of Coulomb collisions between trapped particles, the displacement is proportional to the width of the banana orbit itself, much larger than r_L.

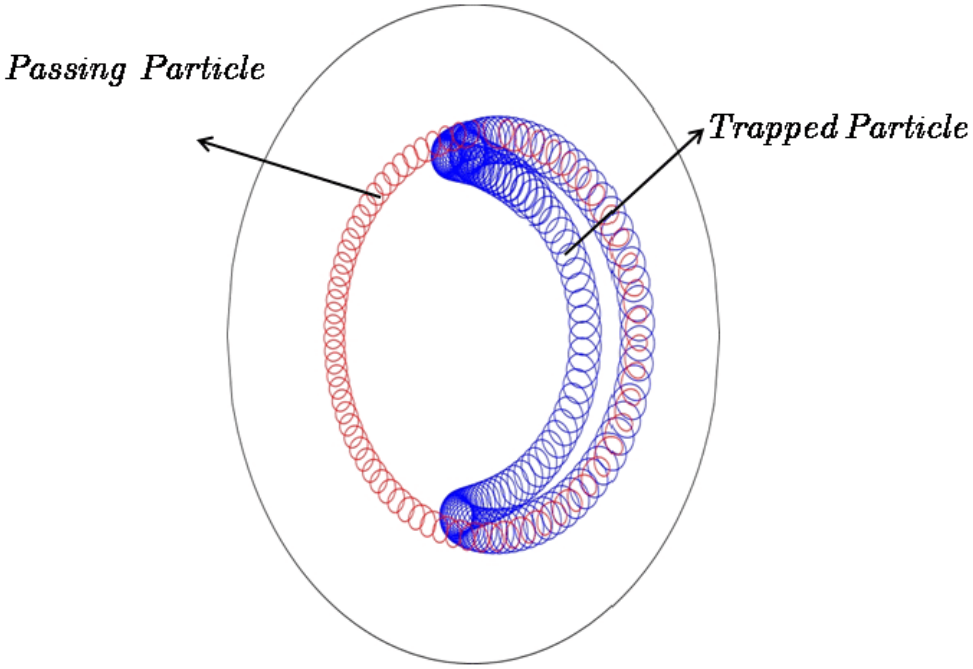

Figure 3.1: Banana Orbit

This description coupling classical transport and effects of toroidal geometry is called neoclassical transport [3].

The increase in neoclassical transport compared to classical levels due to toroidal geometry can be expressed as $D_{neocl} = GD_{class}$, where G is called geometric factor. It depends on the collisional frequency, and therefore on the collisionality. Three different collisional regimes lead to three different values of the geometric factor G. This model estimates a particle diffusivity coefficient D 10-100 times higher than the classical one.

Nevertheless, the neoclassical transport is still driven purely by Coulomb collisions, that is, no anomalous transport due to plasma microscopic instabilities is included. Thus, the neoclassical

transport model represents the minimum level of transport in a tokamak since real coefficients are equal or higher than those estimated in this simpler description.
The following section consists of a short treatment of microscopic instabilities that lead to turbulence. Indeed, a description of turbulent transport mechanisms is necessary to estimate the actual values of the coefficients determining energy and particle confinement in a tokamak.

3.3 Turbulent transport

The significant discrepancy observed between the experimental and expected diffusivity values from neoclassical theory is attributed to turbulent phenomena that can take place in plasmas [6, 7]. The mechanisms that give rise to a turbulent behavior are mainly the fluctuations of the electric field and the perturbations of the topology of magnetic field.

3.3.1 Magnetic turbulence

The equilibrium configuration derived by the MHD model provides that the field lines ergodically cover the magnetic flux surfaces. These surfaces are characterized by constant pressure and, given the high thermal diffusivity, constant temperature.

As previously discussed, in the neoclassical transport model, particles move between one surface and another as a consequence of a Coulomb collision, thus, the radial motion is only provided following this phenomenon. Nevertheless, in a more complex view that includes magnetic perturbations of the ideal equilibrium configuration, lines are disrupted in such a way away from the winding around the toroidal surfaces: in this case, also if the particles follow their orbit according to field lines, a radial transport of different origin may be established.

Studying the transport related to these magnetic perturbations is really challenging because it is possible to observe significant discrepancies with the neoclassical coefficients also in the case in which the perturbation is of the order of

$$\frac{B_{pert}}{B_{eq}} \approx 10^{-4}$$

where B_{pert} is the magnetic perturbation and B_{eq} the unperturbed magnetic field.
The problem of heat and particle transport linked to perturbations in magnetic equilibrium in a

tokamak is deeply related to the topology of the field. Indeed, when the safety factor q is a rational number, a line does not ergodically cover a magnetic flux surface but it closes on itself after a finite number of turns. Surfaces with this characteristic are unstable since a little magnetic perturbation leads to a significant degeneration of the surface itself and so to a chaotic regime.

These perturbations of the magnetic topology lead to a class of plasma instabilities called *macro-instabilities* (or *MHD instabilities*), that are responsible for confinement losses.
One method to characterize the transport induced by magnetic perturbations is to calculate the trajectories along the field lines in that chaotic regime through a random walk approximation [8]. This approach has led to an expression of the particle diffusion coefficient given by

$$D \approx v_{||} D_M$$

where

$$D_M = L_{||} \left(\frac{B_{pert}}{B_{eq}} \right)^2$$

and $L_{||}$ represents the perturbation length along the parallel direction.

3.3.2 Electrostatic turbulence

The most widely adopted approach is based on considering predominantly the electrostatic component of the turbulence. This is a remarkable simplification that neglects magnetic fluctuations.
The plasma within tokamaks is inhomogeneous because of the presence of density and temperature gradients. This drives the formation of an electrostatic potential that leads to another class of plasma instabilities: the *micro-instabilities* (or *drift-wave like instabilities*).

Drift waves

The drift waves [6, 9] are collective plasma oscillation modes driven by density and temperature gradients and by the different ion and electron dynamics.
Consider an initial density perturbation δn along x, that leads to a *diamagnetic drift* velocity:

$$\vec{v_d} = \frac{T}{qBL_n} \widehat{e_y}$$
$$L_n^{-1} = -\frac{\nabla n}{n}$$

in the direction perpendicular to the magnetic field (parallel to $\widehat{e_z}$). The electrons react faster than the ions because of their lighter mass, generating a charge separation and hence an electrostatic potential perturbation, in phase with δn. The resulting electric field $\vec{E}$ leads to a $\vec{E} \times \vec{B}$ drift along the x direction. This causes a flux of less dense plasma towards the more dense region and vice versa, leading to a propagation of the perturbation in the vertical direction.

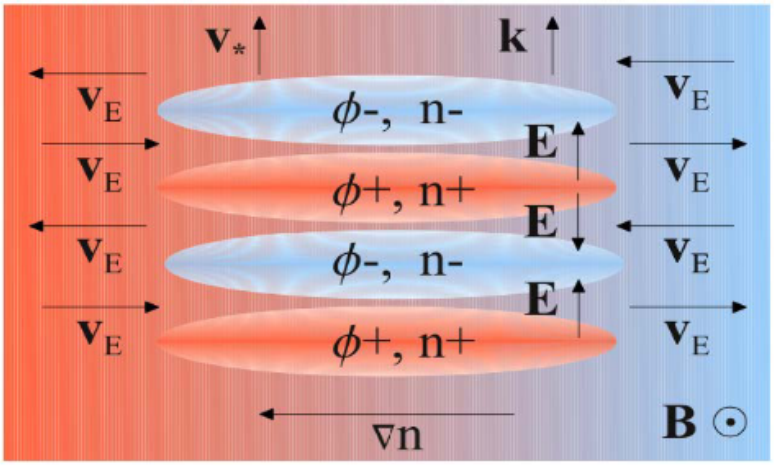

Figure 3.2: Schematic representation of the electron drift wave

***Ion Temperature Gradient* ITG and *Electron Temperature Gradient* ETG**

In the tokamak low-field side, where the ion temperature gradient ∇T_i has the same direction of the magnetic field gradient, a drift wave due to the ion temperature gradient arises. For obvious reasons, these perturbations are called *Ion Temperature Gradient Modes* [10].

Consider an initial ion temperature perturbation δT_i in the tokamak low-field-side. Since the particle drift velocity due to the magnetic field gradient is

$$v \sim ((T_{||})^2 + (T_{\perp})^2)$$

the particles are faster in the hotter region and slower in the colder one. This leads to a density perturbation δn_i which in turn leads to the formation of an electrostatic potential Φ. Thus, with the appearance of an electric field $\vec{E}$, an $\vec{E} \times \vec{B}$ drift occurs. This results in bringing the cold plasma in the colder region and the hot plasma in the hotter region, amplifying the initial density perturbation. The characteristic length of ITG instabilities is of the order of the ion Larmor radius or more.

An analogue mechanism is at the base of ETG micro-instabilities [11], although in this case the initial condition is an electron temperature perturbation T_e that leads to an electron density perturbation δn_e. Unlike ITGs, ETGs develop on the shorter scale of the electron Larmor radius.

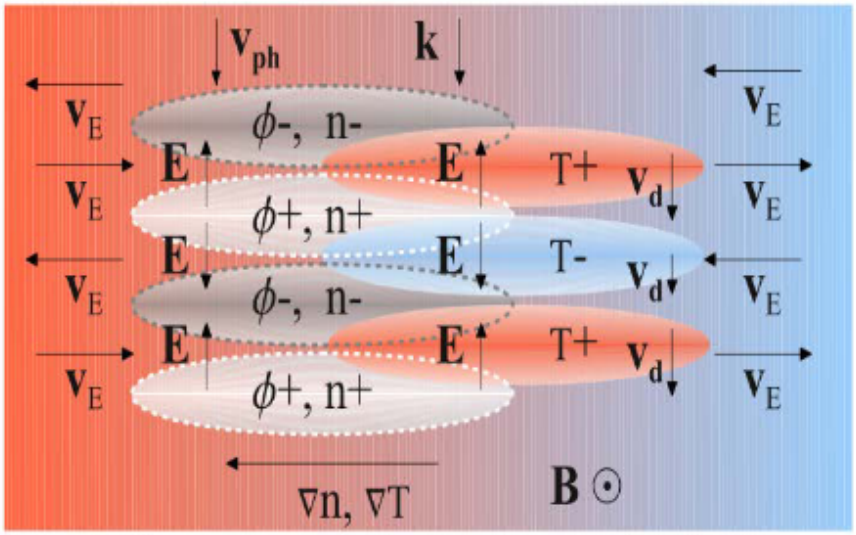

Figure 3.3: Schematic representation of the ITG drift wave

***Trapped Electron Modes* TEM**

A third type of micro-instability depends on the presence within the tokamak of both passing and trapped electrons [12], which respond differently to electrostatic perturbations.
The TEM development is related to both density gradient ∇n_e and electron temperature gradient ∇T_e. Their characteristic length is of the order of the ion Larmor radius as for ITGs.

Critical threshold

In the study of these micro-instabilities it is very interesting to investigate and quantify a critical gradient threshold above which the system becomes unstable.
Through the years, many formulas have been proposed to evaluate threshold values, formulated on the basis of different models and assumptions, as the gyrokinetic model and the fluid model.
The figure 3.4 shows an example of these critical values as a function of density and temperature gradients in the simple case in which $T_e = T_i$.

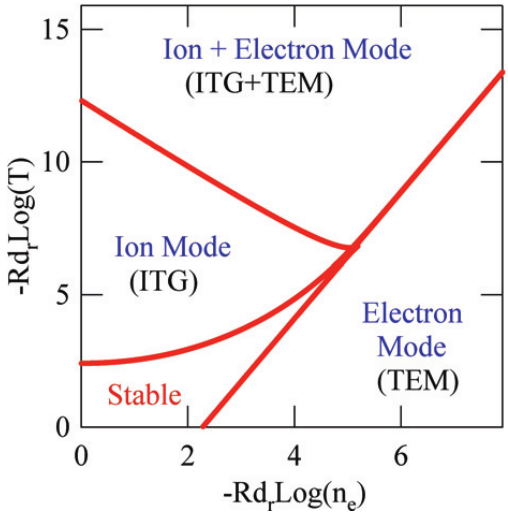

Figure 3.4: Stability thresholds for ITGs and TEMs vs density and temperature gradients

3.3.3 Turbulent transport models

Properly understanding plasma micro-instabilities allows the interpretation and optimization of present-day experiments, predictions concerning future machine performance, and design of control system.

To pursue this goal, many models have been developed, starting from purely empirical ones up to extremely sophisticated kinetic models. The latter have allowed a thorough understanding of the plasma micro-instabilities [13].

As already discussed, the collisional Vlasov equation, coupled with Maxwell equations, accurately describes the temporal evolution of the 6D distribution function of the plasma particles.

Now, consider the entity of the perturbations (δn, δB, δT, etc.) small compared to corresponding background quantities and the fluctuation frequency small with respect to the Larmor frequencies. Then, splitting the distribution function f in an unperturbed part f_0 and a fluctuating part δf, and averaging the Vlasov equation over the Larmor motion, it is possible to derive the 5D *gyrokinetic* (GK) equation [14].

Descending directly from the kinetic equation, the nonlinear GK model provides a physics comprehensive description of turbulent transport, and hence nonlinear GK codes, such as GENE [15], represent the most advance tool to investigate micro-instabilities.

An example of a full-torus gyrokinetic simulation in a tokamak is reported in figure 3.5.

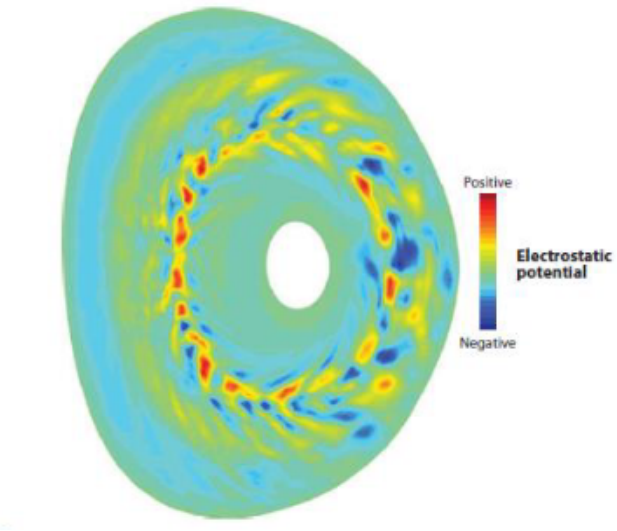

Figure 3.5: Full-torus GK simulation in a tokamak that exhibits an internal transport barrier. The figure displays contours of electrostatic potential. (From Krommes, Ann. Rev. Fluids 2012)

Nevertheless, GK codes are computationally very expensive and thus cannot be used for simulating the whole radial profiles and time evolution of plasma parameters [13].

As consequence, the *quasi-linear (QL) transport models* have been developed. They are based on linearized equations (for example gyrokinetic equations) and hence, thanks to their low computational costs, are faster than GK transport codes.

Nevertheless, QL models require a method to simulate the nonlinear processes that saturate the level of fluctuations. This method consists in applying a *saturation rule*.

A common choice is to use the so-called *mixing-legnth rule*:

$$D \approx \Sigma_k \frac{\gamma_k}{k_\perp^2}$$

where γ_k is the linear growth rate and $k_\perp$ the perpendicular wave number, both associated to fluctuations.

The two most recently developed quasi-linear models are TGLF (Trapped Gyro-Landau Fluid) and QuaLiKiz. The TGLF model [16] solves a set of gyro-Landau fluid equations, taking in account kinetic effects such as the Landau damping and the gyro-averaging. The model can include electromagnetic fluctuations and features both passing and trapped particles and uses the Miller equilibrium to solve shaped geometry with finite aspect ratio. TGLF includes two versions of the

saturation rule: SAT0, a single scale rule, and SAT1, which deals with a nonlinear increase of the critical threshold and multi-scale interactions.

The QuaLiKiz model [18, 19], which is used in this thesis work, is purely electrostatic and is based on the linear eigenvalue code Kinezero [16]. The fundamental part is to linearize the kinetic equations and solve the dispersion relation to find the frequencies for micro-instabilities, namely ITGs, ETGs, and TEMs. The QuaLiKiz quasi-linear expression of the flux is derived by the well-known nonlinear Vlasov equation by averaging over a time τ. The latter must be smaller than the equilibrium evolution time and larger than the characteristic time of the fluctuations. Furthermore, the fluctuating distribution function is assumed to be linearly dependent on the fluctuating electrostatic potential. The resulting linearized equation is compute using Kinezero, taking in account both trapped and passing particles.

After solving the linear problem, the model needs to incorporate nonlinear physics in order to compute particle, momentum and heat fluxes. This is performed using the mixing-length rule.

3.4 Particle sources

The DTT device will be an experimental reactor dedicated to the study the power and particle exhaust (see chapter 2). Then, this tokamak is not meant to be a nuclear power plant, and hence will not operate fusion between D and T. Thus, the particle injection in the Italian project is going to include just dueterium fuelling.

There are essentially three ways to supply plasma with deuterium atoms: Gas Puffing, Neutral Beam Injection (NBI), and Pellet Injection, that will be presented in this section, together with the models used to describe the different particle sources.

3.4.1 Gas puff fuelling

The very first developed fuelling method is the gas puffing, in which neutral molecules are puffed just outside the last closed flux surface, in the Scrape-off Layer region, where they are dissociated. If the resulting atoms are then ionized inside the plasma edge, they fuel the plasma effectively.

The molecular ionization is a two step process as follows:

$$D_2 + e \rightarrow (D_2)^+ + 2e \rightarrow D + D^+ + 2e$$

where both ions and neutrals are produced.

The resulting neutral atoms may undergo a charge-exchange reaction with plasma particles, which have a significantly higher energy than the former. Therefore, once neutralized, they have a better capability to travel inside the plasma core than cold neutrals.

In this context, the evaluation of the mean free path of these *hot neutrals* is fundamental, as well as the reaction cross section. In fact, these two factors heavily influence the neutral penetration and the fuelling efficiency.

The reaction rates of the plasma-neutral interactions that shape the neutral profiles in the SOL depend strongly on both electron density, and electron or ion temperature.

As fluctuations in these fields are highly correlated in the SOL, a turbulence model is necessary to investigate the reaction rates in a proper way.

An example of cross-section profiles performed with a turbulence model is reported in figure 3.6. These cross-section profiles concern the molecular dissociation, the ionization, the charge-exchange reaction, and the two step process previously described.

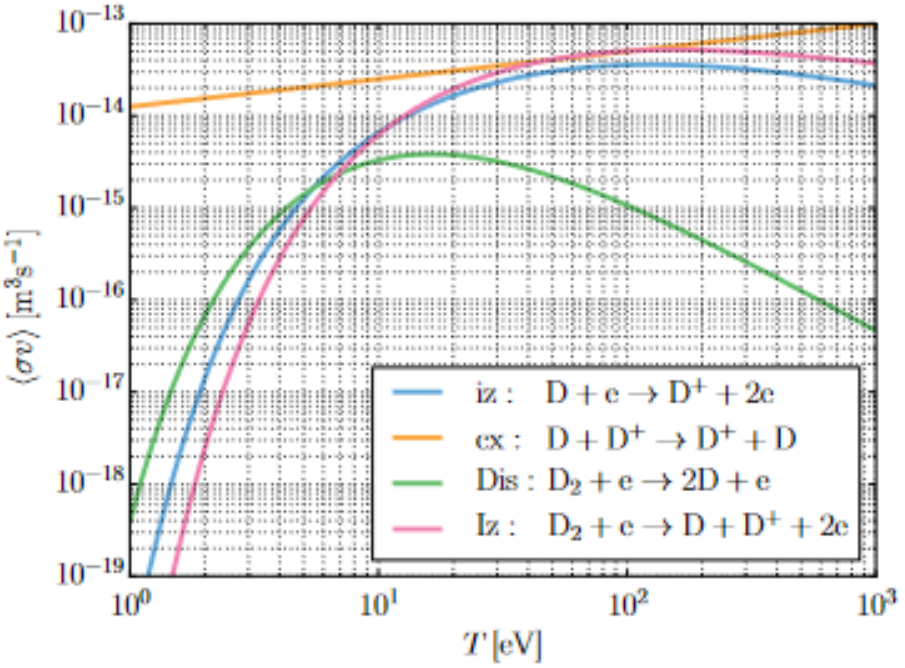

Figure 3.6: Typical reaction rate profiles for plasma-neutral interactions. (From Thrysøe A S, *Simulation of neutrals in a turbulent scrape-off layer*, 2016)

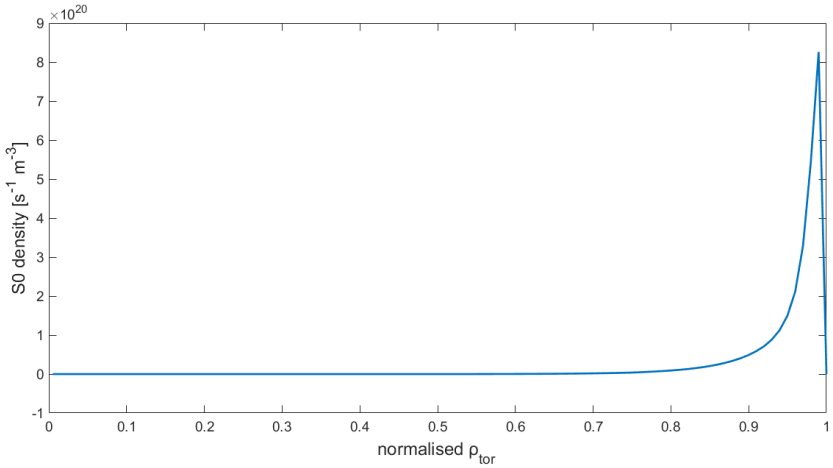

Figure 3.7: Radial profile of the gas puff particle source in DTT

Furthermore, from figure 3.7, that shows a radial profile of the gas puff particle source simulated during this work, it is clear that the neutral penetration into the plasma is adequate for fuelling, since the neutral density rate is significant up to $\rho_{norm} \approx 0.8$.

As in figure 3.7, in any other integrated simulation performed here, the particle source due to the ionization of the neutral atoms is described by FRANTIC [20]. The FRANTIC model performs a very fast 1D neutral gas transport calculation for tokamak core plasmas, taking into account charge-exchange and impact ionization atomic reactions in a simplified nested cylindrical flux surface geometry. The calculation takes as input a neutral source, which can be an ”edge” influx of neutrals representing recycling or gas flow, or a ”volume source” due to recombination and/or the charge exchange halo around injected neutral beams. FRANTIC then calculates neutral density and ”temperature” and toroidal velocity profiles for each of the neutral species associated with the given neutral source. Particle, momentum and energy sources/sinks are calculated, as well as complete particle, momentum and energy balance information for each neutral specie.

3.4.2 *Neutral Beam Injection* NBI

The second method is the well-known NBI, which has already been discussed in the section concerning heating systems. In fact, although the main purpose of Neutral Beam Injection is to raise the plasma temperature well above the maximum achievable ohmic value, it cannot be ignored that it is also, of course, a source of particles for the plasma. See Chapter 2 for its operating principle.
The neutral beam source is a four-stage device. The purpose of the first stage is to produce a source of low-temperature ions, positive or negative. In the DTT project the NBI method is based on accelerating negative ions, that can be produced by standard techniques.
The advantage in creating negative ions over the positive-ion-driven sources is based on the fact that the extra electron is only weakly bound to its neutral atom. Thus, this extra charge can be easily stripped away also at very high energies, resulting in a more efficient neutral atoms production than the one concerning positive ions.
The second stage of the device accelerates the negative ions to a high energy using a high voltage that represents the major part of the input electrical power consumed.
Then, the ions must be neutralized since electrically neutral particles are unaffected by the magnetic field and can travel into the plasma until they are ionized.
The ionization of deuterium atoms takes place across the whole plasma radius, with a distribution as illustrated in Fig.3.8 for a typical DTT plasma.

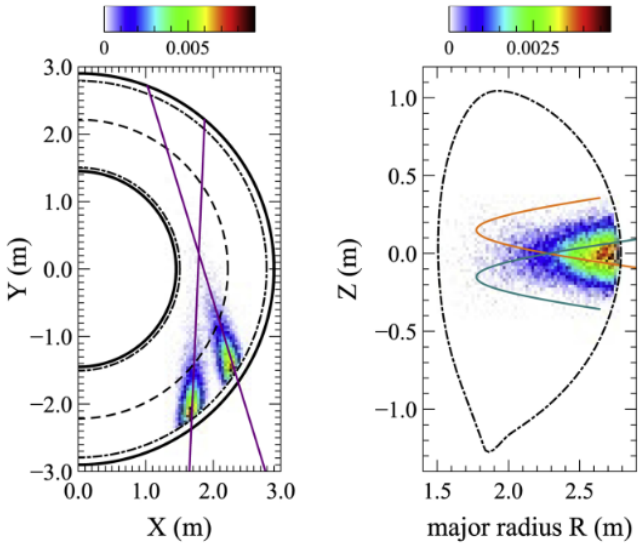

Figure 3.8: D fast ions birth locations in DTT. (From Cecconello M, Fusion Engineering and Design 167 112382, 2021)

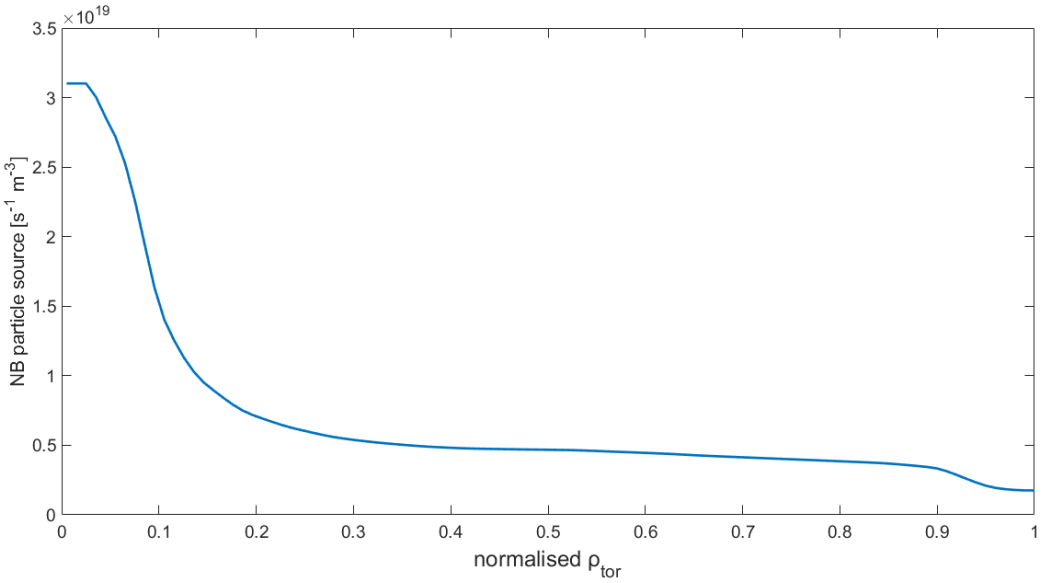

Figure 3.9: Radial profile of the NBI particle source in DTT

Many integrated simulations performed during this thesis work highlight that the neutral beam injection contribution to the neutral source is small compared to gas puffing (figure 3.9).

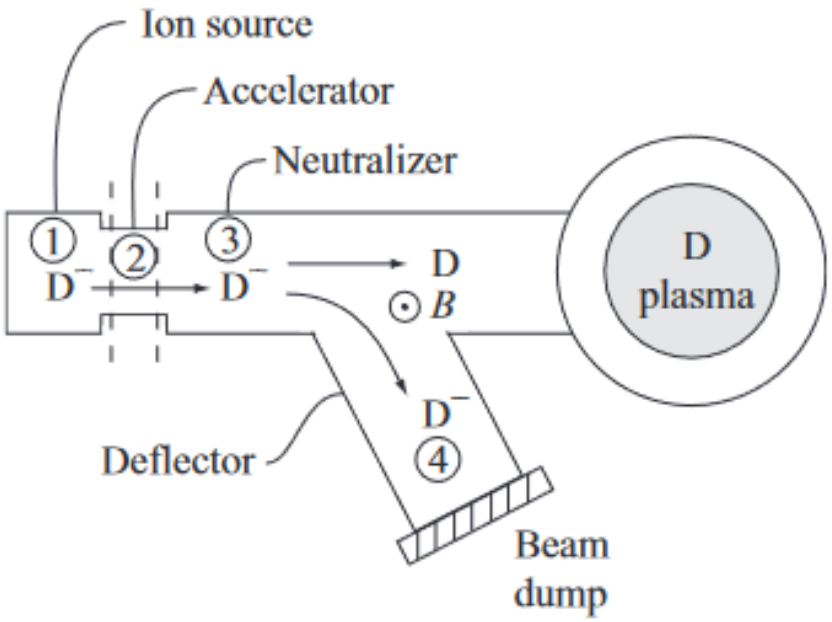

Figure 3.10: Schematic diagram of a neutral beam system: (1) ion source, (2) accelerating region, (3) neutralizer, (4) charged particle deflector

3.4.3 Pellet Injection

High-speed injection of solid fuel was first proposed in 1954 as a possible solution to the problem of transporting fresh fuel across the confining magnetic fields into the plasma of a fusion reactor. After studies over a few decades, injection of cryogenic pellets has become a common practice in tokamaks and stellarators to refuel the plasma. Typically, the devices used for the injection operate at very low temperatures ($\sim$ 10 to 20 K) and accelerate the pellets up to the speed of 3000 m/s. Pellets are small solid fuel elements with a radial size of the order of millimeters ($\sim$0.4 to 6 mm) that are injected with high speed to deposit particles as closely as possible to the plasma core. This technique was introduced because of its high fuelling efficiency and particle confinement with respect to the conventional method via gas puffing.

The description of the fuelling due to pellet injection requires the modelling of three mechanisms: the ablation of the pellet material, the expansion of the charged cloud along the magnetic field lines, and the $E \times B$ and ∇B drifts that quickly displaces the cloud towards the low-filed side, driving the final deposition profile.

Ablation process and Plasmoid homogenisation

Most of the nowadays used pellet ablation models are of the NGPS [21] type (Neutral Gas and Plasma Shielding), in which the pellet is assumed to be surrounded and shielded by a layer of ablated particles that are gradually ionised.

Once the pellet enters the edge and penetrates into the plasma core, close to the pellet surface, the temperature is of the order of a small fraction of an electron volt. Thus, the boundary particles are still non-ionized and bound together to form molecules. This results in a shield against the plasma heat flux q_n, that is, just a part q_p of this total flux will actually be available to vaporize the frozen molecules.

As a consequence, this fraction will initially vaporize and partially ionized only the outer particles, which will form a charged cloud, the so-called plasmoid, in which the neutral pellet is immersed. The formation of this cloud is modelled by a set of differential equations reported in [22].

The plasmoid can be considered independent from the rest of the pellet since it is composed by charged particles, and hence it is stopped by the magnetic field or drifted away by the $E \times B$ and ∇B drifts caused by the magnetic filed gradient and pressure inhomogeneity. Then, the particles in the ablation cloud freely homogenise in the plasma.

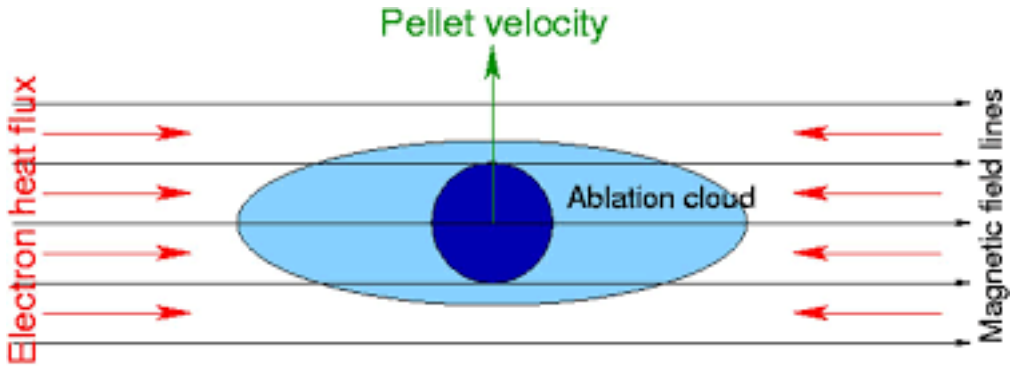

Figure 3.11: Pellet during the ablation process

The NGPS model features a description of the pellet evaporation and cloud expansion without taking into account the fast ∇B-induced drift, which is the dominant mechanism that leads to the final pellet deposition profile.

A more complete ablation/deposition model is HPI2 [23], which includes the ∇B-induced drift and

combines a number of features that are only selectively available in other pellet source models, such as the self-consistently calculation of the 2D magnetic flux surface geometry.

Pellet injection position

Pellet injection will be one of the primary methods to refuel the DTT plasma with deuterium atoms. There are two main injection positions that have been valuated in order to maximize the fuelling efficiency (defined as the fraction of the pellet initial mass that remains inside the plasma): *Low Field Side* (LFS), from the outside midplane, and *High Field Side* (HFS).
In the latter injection scheme, curved guide tubes are used to route the pellets from the injector to locations on the inner wall of the torus.
Although in large devices HFS injection is mandatory because the drift displacement of the pellet particles following the ablation process is of the order of pellet penetration, for medium device as DTT, both HFS and LFS are achievable.
In this context, different injection lines are investigated in the Pégourié report [24] for DTT and they are summarized here.

Injection line	R_{inj} (m)	Z_{inj} (m)	θ	R_C (m)
LFS	2.73	0.00	-90°	0.00
VHFS	1.80	1.02	0	0.00
HFS	1.40	0.00	90°	0.10
OHFS	1.40	0.24	41°	0.40

Table 3.1

(LFS: Low Field Side - VHFS: Vertical high Field Side - HFS: High Field Side - OHFS: Oblique High Field Side)

where R_C is the curvature radius of the curved guide tube, Z_{inj} is the injection height compared to the midplane, θ is the injection angle, and R_{inj} the distance from the center of the torus at which the pellet is injected.
Simulations performed using the ablation/deposition model HPI2 have shown that OHFS injection line leads to a higher fuelling efficiency (up to 0.95) with respect to other positions, and hence will be the one considered for this work.

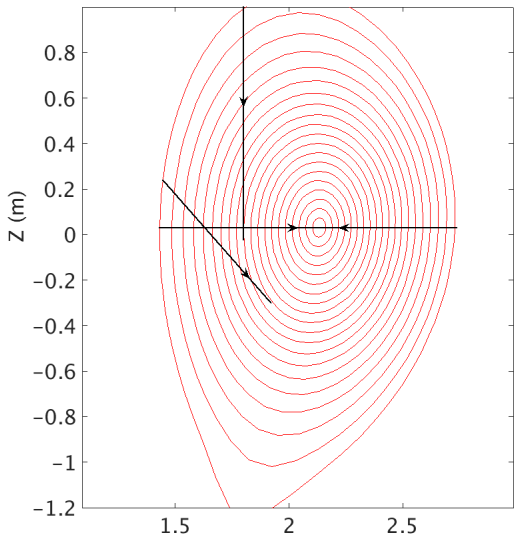

Figure 3.12: Geometry of the different injection lines considered. (From Pégourié report, 2020)

Chapter 4

Integrated modelling of a tokamak plasma

The behaviour of a plasma in a tokamak is very complex due to many different physics processes coupled to each other, e.g. MHD equilibrium, turbulent transport, effect of impurities, plasma-wall interactions, heating and fuelling, and other phenomena. Many detailed codes exist in order to describe each aspect of the tokamak and their non-linear interactions.

With the term *integrated modelling* we refer to simulations in which many different aspects related to plasma within tokamaks are modeled self-consistently. This is especially important for studying nonlinear multi-channel interactions and for scenario modelling, prediction and optimization.

In this thesis work, integrated simulations have been made with the JINTRAC transport code suite [25] and the QuaLiKiz model.

4.1 The JINTRAC suite of codes

JINTRAC is a system of 25 physics-modules for the integrated modelling of complex tokamak scenarios, involving simultaneous simulations of different regions of the reactor.
As already discussed, in a tokamak, the magnetic pressure due to the poloidal and toroidal magnetic field balances the plasma pressure in order to achieve a static equilibrium (see chapter 2). Thus, the equilibrium condition depends on the interaction between an externally imposed field and the thermal pressure of the plasma: a magnetic field equilibrium code is therefore required in any scenario modelling suite. In JINTRAC, the codes adopted are three: EFIT [26], CREATE-NL [27] and ESCO, a simplified fixed boundary solver.

Furthermore, these simulations need to solve transport equations for heat, particle and momentum for both main species and impurities. Consequently, the 1.5D transport solver JETTO [28] is coupled with the impurity code, and both with the equilibrium one. In JINTRAC runs, the distribution of the different ionization states of the impurities is calculated by SANCO [29], using neoclassical and turbulent transport from Romanelli-Ottaviani [30] and QuaLiKiz models, respectively.
Another important issue to deal with is particle fuelling. The modelling hence requires the coupling between particle source codes and JETTO. To calculate the neutral source due to gas puffing, the FRANTIC code has been included in JINTRAC, as well as both HPI2 and NGPS models for evaluating the ablation/deposition process following a pellet injection.
Other aspects included in simulations are the external auxiliary heating and current drive, in order to predict the heating profiles, as well as all nonlinear interactions between heating and plasma and between the different transport channels. The RF antenna, NNBI injectors, and ECRH systems have been developed in the JINTRAC suite of codes, and the relative power deposition profiles are calculated by PION [31], PENCIL [32], and GRAY [33] codes, respectively. In addition, the JINTRAC suite includes an extensive range of models for radiation, fusion reactions, MHD instabilities, etc.
A code dealing with transport in the scrape-off layer is also coupled to the JINTRAC suite, but this has not been used for this thesis work, which deals only with the plasma inside the separatrix.

4.1.1 The 1.5D transport solver JETTO

JETTO is a 1.5D core plasma fluid code which solves the plasma transport equations averaged over magnetic surfaces calculated by the Grad-Shafranov equilibrium equation. It is the central part of the integrated transport code suite JINTRAC, and has been designed to calculate plasma profiles within the separatrix, using QuaLiKiz as turbulent transport model and NCLASS [34] as neoclassical one.
JETTO's mathematical structure involves a consistent set of equations that deals with most of transport problems of interest for DTT and other tokamaks. In fact, the complete set includes equations for ion and electron densities and temperatures, impurity densities, toroidal rotation and plasma current.
In JETTO, electron and main fuel ion equations are solved on a regular grid, allowing to use a

finite-difference method. Impurity densities are derived by mass continuity equations for impurities solved by SANCO. The time step used is the same as the transport solver, while the grid is irregular since higher resolution is required in the edge of the plasma, where atomic processes are important. In addition, JETTO fully integrates solvers for particle sources, like FRANTIC, and for pellet ablation/deposition calculation, like NGPS and HPI2 (see chapter 3).

In the JETTO whole set of equations, the standard source and sink terms are related to auxiliary heating systems, making it necessary to combine the transport solver with proper codes that compute the appropriate power deposition profiles, such as the mentioned PION, PENCIL, and GRAY.

ESCO, the equilibrium code, is called within JETTO on a frequency selected by the user. In order to solve the coupled equilibrium and transport equations consistently, a *splitting technique* [35] is applied, dividing the global set of equations in smaller subsets concerning distinct phenomena, and assuming the boundary and the initial conditions of each subset independent from the others. Then, consistently with this assumption, the coupled equilibrium and transport set of equations is solved in two steps. First of all, an equilibrium calculation is performed. The inputs for this computation are plasma pressure and current profiles, and are passed to ESCO from the transport solver. Then, the equilibrium code solves the Grad-Shafranov equation and returns the magnetic surface configuration and new pressure and current profiles. At the end, a self-consistent transport simulation that includes these ESCO outputs is computed.

Furthermore, models are integrated in JETTO to take into account edge physics. Indeed, transport models for the plasma core mentioned many times are unsuitable to model the transport in the pedestal region. Moreover, frequent MHD instabilities affecting the plasma edge lead to perturbations called *Edge-Localized Modes* (ELMs) [36], making it necessary to simulate these disruptions.

The simplest analytical model incorporated in JETTO is based on adjusting transport coefficients when the normalized pressure gradient exceeds a critical threshold [37]. Basically, D and $\chi_{e,i}$ are calculated as

$$D = D^{neocl} + C_1 \cdot max\left(0, \frac{\alpha_{max}}{\alpha_c} - 1\right)^{\beta}$$

$$\chi_{e,i} = \chi_{e,i}^{neocl} + C_{2,3} \cdot max\left(0, \frac{\alpha_{max}}{\alpha_c} - 1\right)^{\beta}$$

where D^{neocl} and χ^{neocl} are the neoclassical diffusivity and thermal conductivity, $C_{1,2,3}$ and β are constants, α_{max} is the maximum normalized pressure gradient inside the transport barrier, and α_c

represents the critical pressure gradient threshold beyond which ELM crashes occur.

4.2 Multi-channel integrated modelling in support to the DTT project

This thesis work has contributed to the integrated modelling of full power DTT ($R = 2.14\,m$, $a = 0.65\,m$, $B_t = 6\,T$, $I_p = 5.5\,MA$) scenarios in H-mode, presented in [38] and briefly summarized here. These simulations solve the transport equations for heat, particle and momentum in a self-consistent magnetic equilibrium, leading to the prediction of radial profiles concerning the electron and ion temperatures, main density, impurity densities, current density, and toroidal rotation. Integrated runs have been performed in the JINTRAC suite of codes using the 1.5D transport solver JETTO (see 4.1).

This integrated modelling of DTT deuterium plasmas concerns the region inside the separatrix. The transport equations are initially solved up to $\rho_{tor} = 0.94$, where $\rho_{tor} = \sqrt{\frac{(\Phi/\pi B_{tor})}{(\Phi/\pi B_{tor})_{max}}}$ is the normalised minor radius, while the physics within $0.94 < \rho_{tor} < 1$, the pedestal region, is solved outside JINTRAC by the Europed code [39] with the EPED1 model [40]. The values at the top of the edge pedestal are therefore used as boundary conditions for the predictive simulations within $\rho_{tor} = 0.94$.

Subsequently, the transport equations are solved up to the separatrix, performing self-consistent simulations of the pedestal physics and trying to match the values obtained by Europed. This second part has been carried out within this thesis work, in order to determine the deuterium fuelling needed to support the desired plasma density, as discussed in detail in the next chapter.

Inside the plasma core, the turbulent transport is calculated by the QuaLiKiz quasi-linear transport model. Nevertheless, in order to tune plasma parameters in a faster way, in the very first part of the work, the QuaLiKiz Neural Network (QLKNN) [41] has been used (less computational costs).

It is mostly suitable to replicate QLK profiles at the plasma edge, and hence is properly adequate to tune the pedestal quickly, while the inner part presents a discrepancy up to 15 per cent with respect to the complete version, as shown in figure 4.1. QLKNN, as well as QLK, is integrated in the 1.5D transport solver JETTO.

For these JETTO simulations, the MHD equilibrium is self-consistently calculated by ESCO

three times per second, while the plasma boundary is kept fixed and previously calculated using CREATE-NL.

Auxiliary heating and current drive are also modelled self-consistently in the JINTRAC suite of codes using the solvers mentioned in 4.1, except for the ECRH module, calculated separately by the code GRAY and added to the integrated modelling as ex-file.

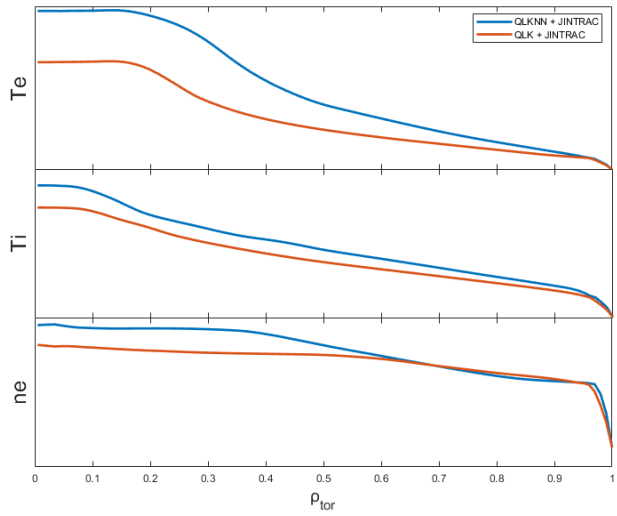

Figure 4.1: QLK vs QLKNN T_e, T_i and n_e profiles simulated during this thesis work.

The ICRH system is meant to operate in the frequency range 60-90 MHz. It is composed of modular units, each one with 2 RF antennas. In these simulations, the frequency is set to 90 MHz and each module provides a power of 4 MW. Moreover, the full power heating mix involves 1 NBI injector, providing to the plasma $\sim$ 10MW through a 500 keV Deuterium beam.

Figure 4.2 shows radial power deposition profiles for ICRH, ECRH, and NBI heating. We can observe a good power penetration into the plasma core in all three cases.

The impurities included in this integrated modelling are Argon (Ar, A$\approx$40, Z=18) and Tungsten (W, A$\approx$184, Z=74). Argon is a seeding gas used to enlarge the radiative dissipation in order to decrease the divertor thermal load, while Tungsten comes directly from the divertor surface. Their density profiles and radiation are modelled by SANCO, setting a radially constant $Z_{eff} = \sum_s Z_s^2 n_s/n_e = 1.7$ (effective charge) and a density ratio $n_w/n_{Ar} = 0.05$ as initial conditions. In figure 4.3, the density profiles for impurities and the Z_eff profile are displayed, where we can observe some penetration of both impurities within the plasma core.

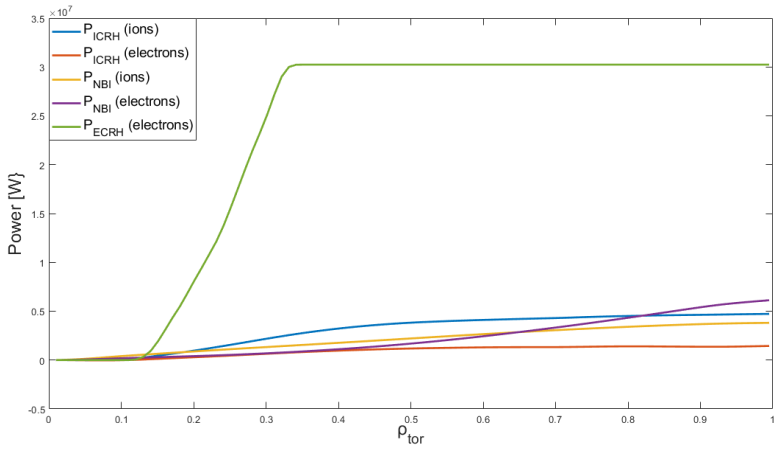

Figure 4.2: Radial profiles of: ICRH power deposited to ions and electrons, NBI power deposited to ions and electrons, ECRH power deposited to electrons.

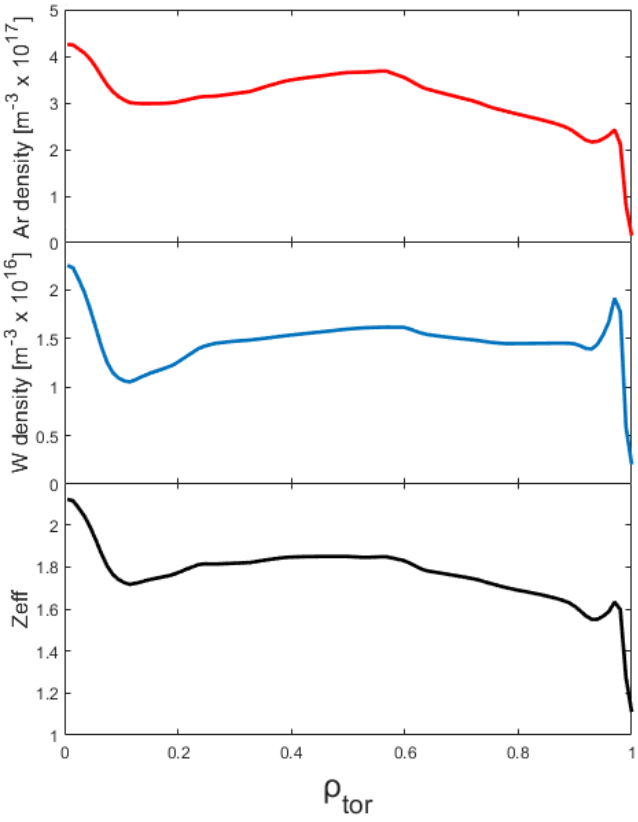

Figure 4.3: Starting from the top: radial density profile for Argon, radial density profile for Tungsten, effective charge profile.

This multi-channel integrated modelling will be particularly useful to support the design of the device and to provide reference radial profiles for diagnostic studies and estimation of particle losses. Furthermore, results from these integrated runs led to the decision to enlarge the tokamak up to R=2.19 and a=0.70 [38].

The next chapter will be focused on the discussion concerning deuterium fuelling, the core part of this thesis work.

Chapter 5

Predictive simulations of DTT fuelling

In order to investigate for the first time the deuterium fuelling and the plasma response to particle injection in the DTT plasma, a work of predictive simulations regarding the fuelling methods discussed in 3.4 was needed. This work started from reference profiles with fixed pedestal, in which transport equations were solved up to $\rho_{tor} = 0.94$ and the plasma edge calculated by the Europed code with the EPED1 model. The purpose was to reproduce these profiles solving the equations up to $\rho_{tor} = 1$, studying and optimizing the particle sources required to sustain the pedestal density. The work was split into three parts. The first one concerned integrated simulations in the old DTT configuration ($R = 2.14\,m$ and $a = 0.65\,m$) with gas puff as fuelling method, evaluating the level of neutral flux at the separatrix required to sustain the pedestal density. In this context, particular emphasis was given to assess if the nominal gas puff rate was higher than the applicability limits, in order not to have extreme fluxes that lead to the degradation of the plasma edge.

The second section dealt with predictive simulations of pellet fuelling, considering DTT of the same size, and taking into account different pellet dimensions and velocities, in accordance with the Pégourié report [24]. An assessment of the injection frequency was made in order to establish the feasibility of this fuelling method, according to the limits imposed by the injectors. A constraint to avoid too large density perturbations that would cause problems to the heating systems, particularly ECH, was taken into account for this evaluation.

At the end, since the integrated modelling to which this thesis work belongs led to the decision to enlarge the DTT device up to $R = 2.19\,m$ and $a = 0.70\,m$, predictive simulations of gas puff fuelling were carried out also in this new device configuration.

In order to solve the transport equations within the separatrix, JETTO was used, with QuaLiKiz and QuaLiKiz Neural Network as turbulent transport models over the whole profile. Moreover, in the pedestal region models that simulate the Edge-localized modes were exploited.

The general settings concerning auxiliary heating, impurity densities, and equilibrium were the same as those presented in section 4.2 and used in the integrated plasma modelling within $\rho_{tor} < 0.94$.

5.1 Fuelling by Deuterium gas puff

The results of full power integrated simulations with predicted pedestal and gas puff fuelling are presented in this section.

In order to replicate the fixed pedestal of the reference profiles, specific values for the pedestal electron density n_e and temperatures T_e, T_i needed to be achieved in the simulation, and hence the ELM *Continuous(TOB)* (**T**op **O**f **B**arrier) model was more convenient to use compared to the Continuous(α_c) model presented in 4.1.1. In fact, with the former, additional contributions to D, χ_e, χ_i in the transport barrier are calculated independently as function of $n_{e,TOB} - n^T_{e,TOB}$, $T_{e,TOB} - T^T_{e,TOB}$, $T_{i,TOB} - T^T_{i,TOB}$, respectively, where $n^T_{e,TOB}$, $T^T_{e,TOB}$, and $T^T_{i,TOB}$ are the target values for the pedestal top that need to be specified in the ELM settings panel instead of the α_c value.

These target values, chosen equal to those obtained using the EPED1 model, were set to:

$$n^T_{e,TOB} = 1.4 \cdot 10^{14}\ cm^{-3}$$

$$T^T_{e,TOB} = 2200\ eV$$

$$T^T_{i,TOB} = 2200\ eV$$

The boundary conditions were imposed at the separatrix and kept constant during the running time, choosing the same values of the Europed run:

$$I_p = -5.5\ MA$$

$$T_i = T_e = 100\ eV$$

$$n_e = 0.32 \cdot 10^{14}\ cm^{-3}$$

where I_p is the plasma current.

The work started with the tuning of the ETB, varying the pedestal width and smoothing in order to

reproduce the Europed profiles. The width can be set by specifying the variable *RHONTOB* in the JETTO settings panel, so as to decide the top of the barrier position in terms of ρ_{tor}. Alternatively, it can also be defined in centimeters in the Edge Transport Barrier panel.

On the other hand, the smoothing can be set in terms of normalized minor radius specifying the variable *SMTHRHON*. It represents the width in which the smoothing algorithm is applied, once from the top of the pedestal towards the core and another from the top of the pedestal towards the edge. Internally, this width is converted into a number of grid points.

The neutral particle input was modelled by FRANTIC. A feedback mechanism for neutral injection was implemented so that the particle input switched on at its nominal rate every time the density at the top of the ETB dropped below $n^T_{e,TOB}$.

The work started from tuning the pedestal width and smoothing, keeping the nominal rate initially constant at the arbitrary value of $8 \cdot 10^{21}\ s^{-1}$. These first simulations led to the decision to set RHONTOB=0.96 and SMTHRHON=0.02. The results reported here were obtained with JETTO equipped with QLKNN (figure 5.1) and QLK (figure 5.2).

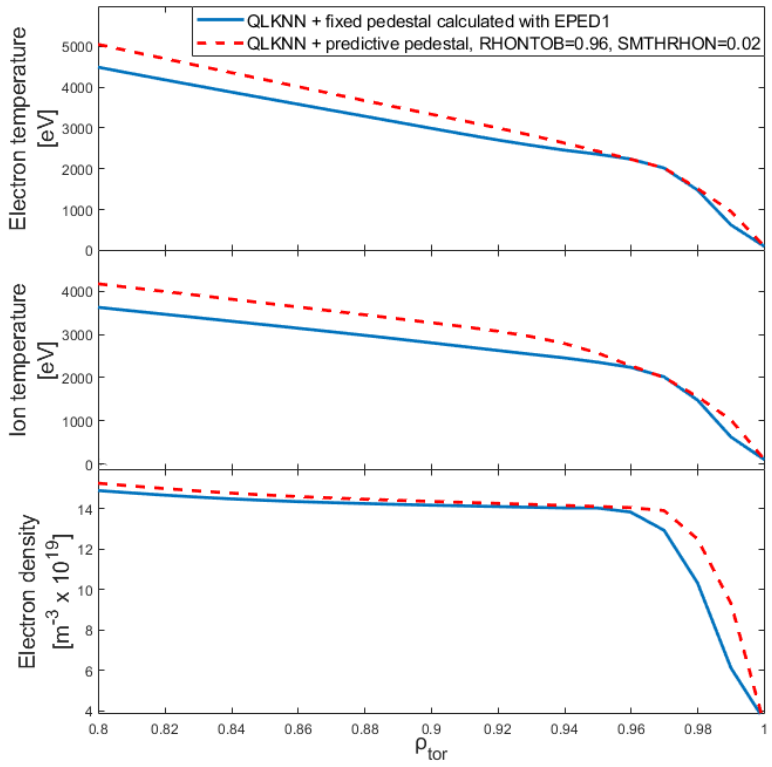

Figure 5.1: Fixed (blue line) vs predictive (red line) pedestal using QuaLiKiz Neural Network as turbulent transport model.

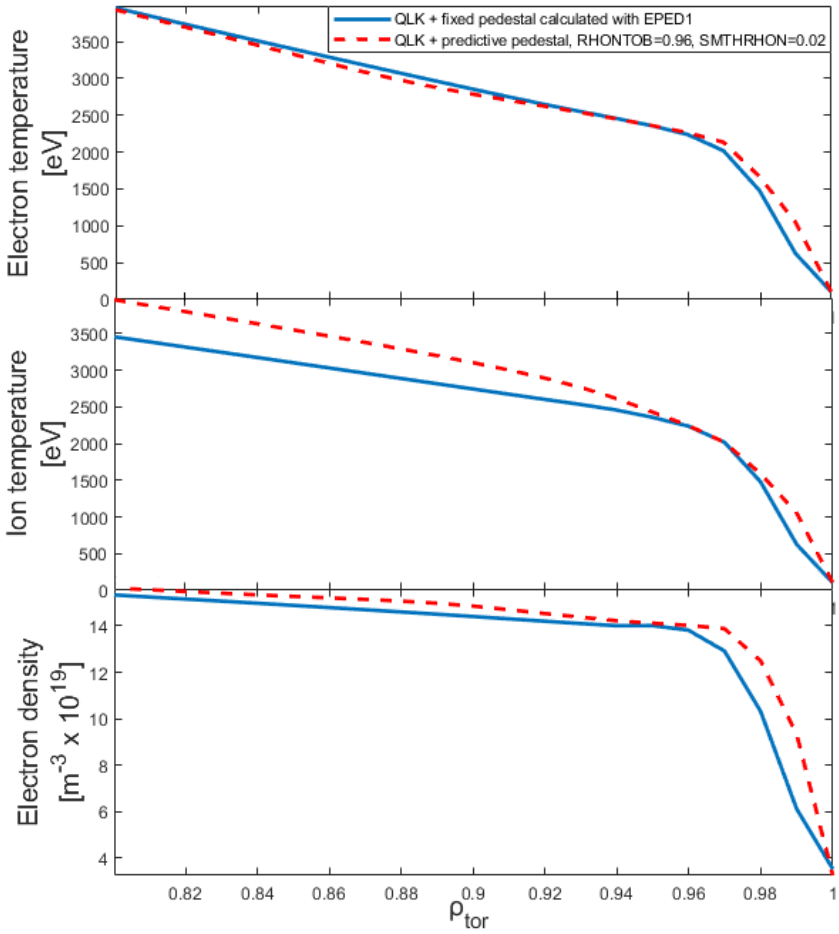

Figure 5.2: Fixed (blue line) vs predictive (red line) pedestal using QuaLiKiz as turbulent transport model.

As you can see from figures 5.1 and 5.2, these integrated runs accurately reproduced the temperature profiles with fixed pedestal, while the density ETB seems to be slightly narrower. Nevertheless, the choice of these values for RHONTOB and SMTHRHON represents the fair trade-off in order to achieve acceptable results for the three profiles simultaneously.
On the other hand, figure 5.3 emphasizes once again how effectively QLK and QLKNN produce similar profiles regarding the external region, and therefore the lower computational cost of QLKNN is of enormous help in works concerning the pedestal tuning.

As previously introduced, we started from an arbitrary nominal rate of $8 \cdot 10^{21}\ s^{-1}$. However, in figure 5.4, we can see that this value is too high. In fact, the neutral source presents an extremely oscillating trend and has actually a much lower average value (horizontal red line).

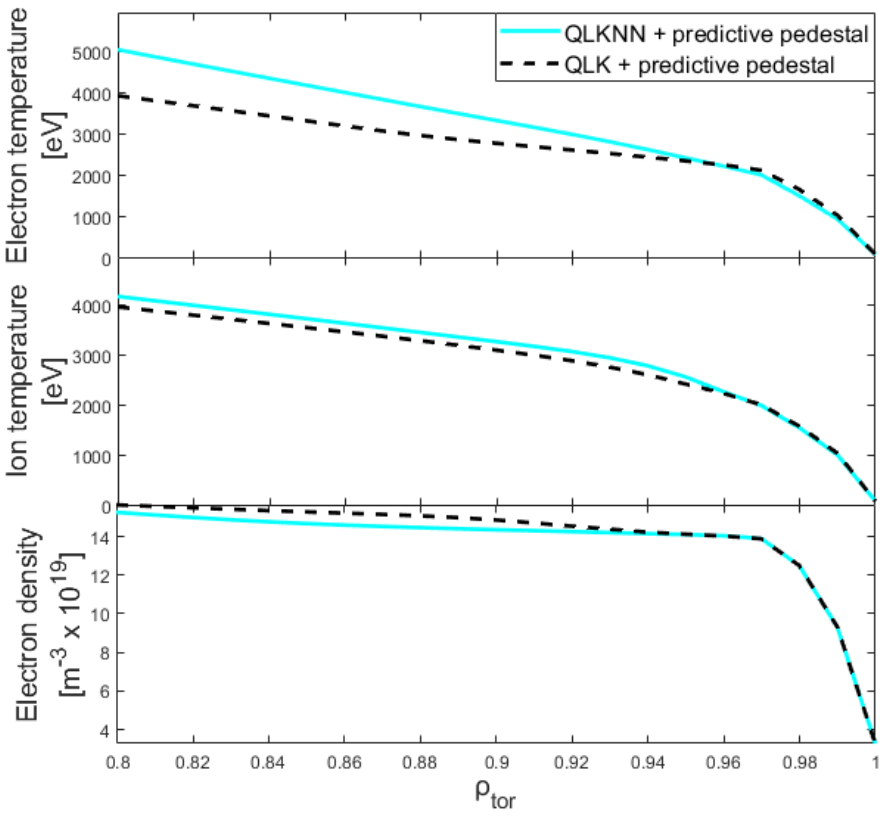

Figure 5.3: QLKNN (pale blue line) vs QLK (black line) pedestal.

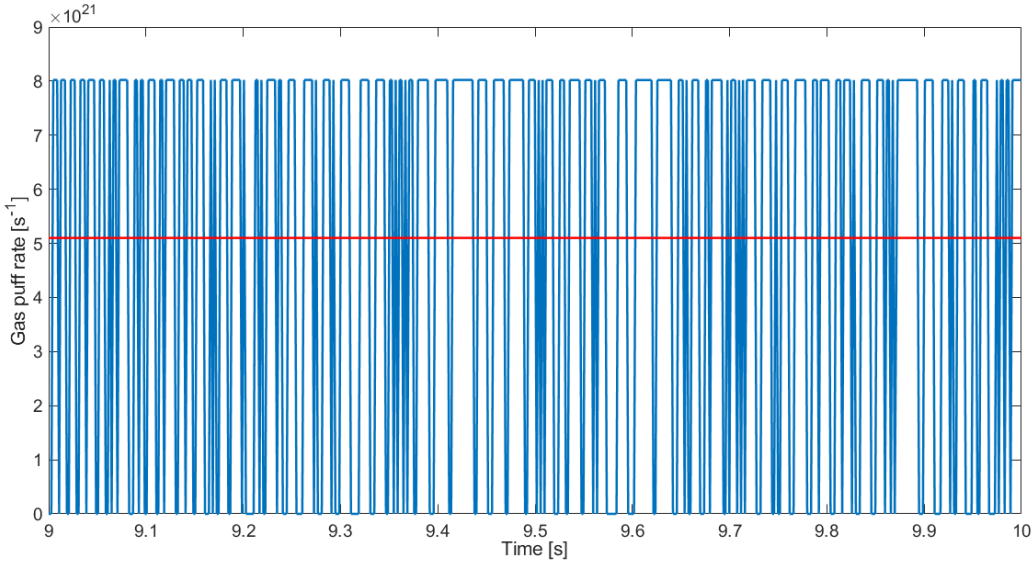

Figure 5.4: Gas puff rate (blue line) and its average value (red line). PPF number: 1211.

Nevertheless, the initial nominal value of $8 \cdot 10^{22}\ s^{-1}$ is unsuitable to assess if the rate is too high compared to the maximum achievable. In fact, the feasibility limit must be compared with the minimum gas puff value capable of sustaining the pedestal density, that is the nominal rate at which the neutral injection system stays on most of the running time. Therefore, a tuning work concerning the gas puff input was required.

The job started from the results obtained with the initial pedestal tuning, and proceeded by launching successive simulations in which the previous nominal rate input was progressively replaced by its average value, until the gas puff rate stabilized around its nominal value. Figure 5.5 shows the final result in which the input source stays on most of the running time at the nominal value of $\sim 4 \cdot 10^{21}\ s^{-1}$.

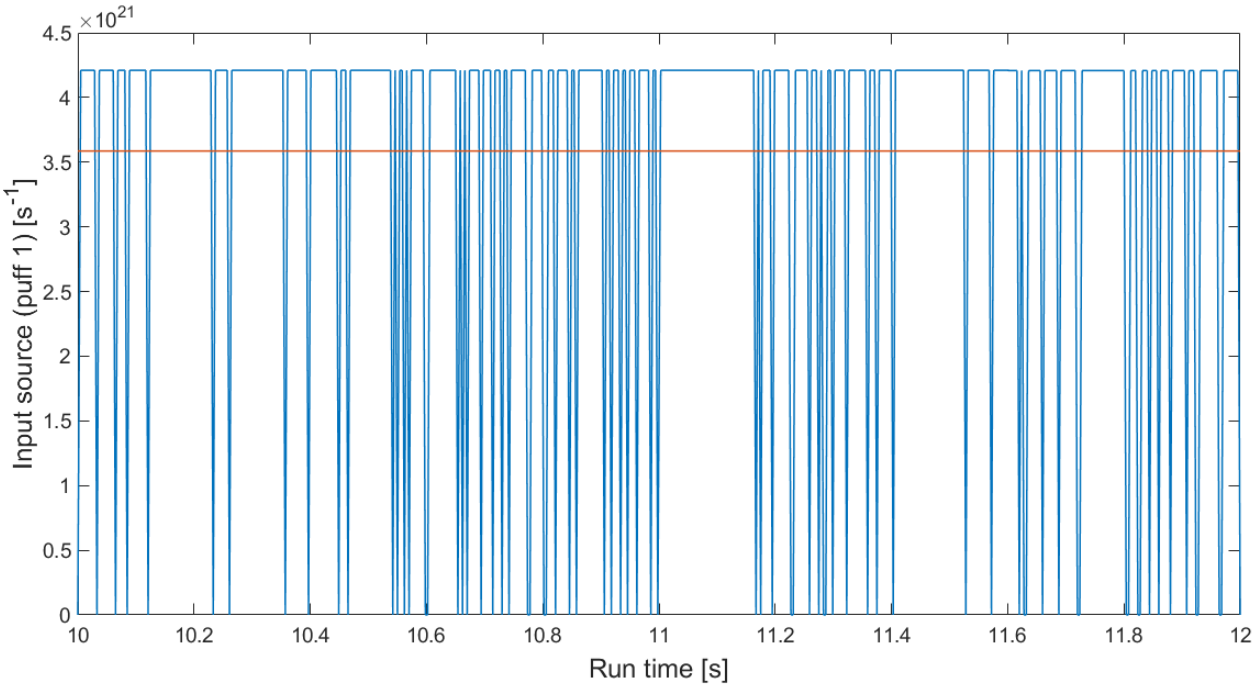

Figure 5.5: Gas puff rate (blue line) and its average value (red line). PPF number: 1243.

In figure 5.6, the T_e, T_i, and n_e radial profiles resulting from this final adjustment work are compared to the profiles of the QLK case with fixed pedestal to show the good agreement between them.

The neutral penetration into the plasma evaluated by FRANTIC is adequate for fuelling, since the neutral density rate is significant up to $\rho_{tor} \sim 0.8$, as displayed in figure 5.7. A time average of

figure 5.5 yields that a neutral flux level of about $0.36 \cdot 10^{22}$ particles/s at the separatrix is required.

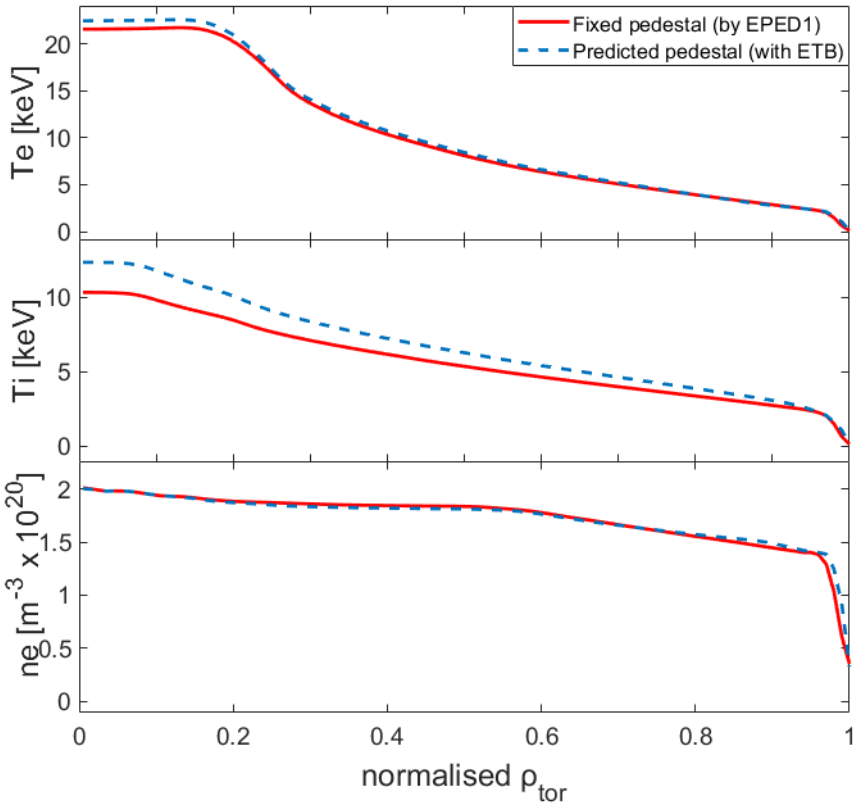

Figure 5.6: Radial profiles. PPF number: 1243.

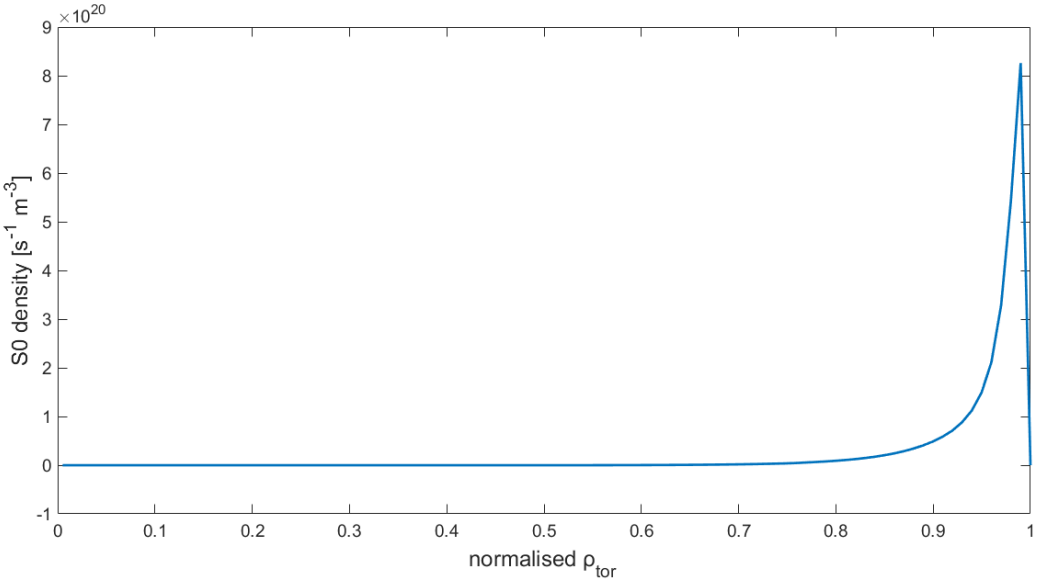

Figure 5.7: Radial profile of the source of neutrals from the edge. PPF number: 1243.

The dependence of neutral penetration across the separatrix as a function of deuterium fuelling was found starting from results obtained in [42] with the edge code SOLEDGE2D-EIRENE[43]. This study underlined the need to operate with nominal gas puff rate of $\sim 5 \cdot 10^{22}$ particles/s in order to achieve the deuterium fuelling levels corresponding to the required neutral flux at the separatrix. Since this value is near to the feasibility limits for the gas puffing and pumping systems, a pellet injection system is recommended in order to avoid degradation of the plasma edge and minimize the operational risk.

5.2 Fuelling by Deuterium pellets

As pointed out in the previous section, the development of a pellet fuelling system is recommended in order to mitigate risks related to high puff rates. Therefore, a work of integrated simulations including pellet injection was necessary.

This work started accordingly to what Pégourié presented in his report [24], in which pellet deposition profiles in three realistic OHFS configurations (**1**: $Z_{inj} \sim 1.5$ m, $R_c = 15$ cm; **2**: $Z_{inj} \sim 0.4$ m, $R_c = 15$ cm; **3**: $Z_{inj} \sim 0.3$ m, $R_c = 40$ cm) were simulated using the ablation/deposition model HPI2. Although the results showed that the three positions are equivalent concerning fuelling efficiency and pellet penetration depth, the choice fell on position 3 for technical considerations. Then, this configuration was implemented in JETTO and therefore used in this work.

In these JINTRAC runs, the pellet particle source profiles were obtained by running the HPI2 code, taking into account three different choices for pellet size and velocity:

- $r = 0.7\ mm$; $v_p = 617\ m/s$;
- $r = 1\ mm$; $v_p = 516\ m/s$;
- $r = 1.3\ mm$; $v_p = 640\ m/s$.

where r is the pellet radius and v_p the pellet injection velocity. According again to the Pégourié report, these pellet sizes were determined by requiring that the local electron density increment due to the pellet is < 20 % of the pre-injection value, while the injection velocity v_p scaling law with r resulted from studying the ice critical yield strength in two approximations for the pellet motion inside the guide tube: slipping and bouncing.

Basically, most of the general settings used in gas puff simulations have been maintained. Nevertheless, the idea to fix a density target at the top of the barrier is unsuitable when the purpose is to study the density evolution due to the pellet injection. Thus, the Continuous(TOB) model was replaced by the Continuous(α_c) model in the ELMs recipe. As a consequence, a tuning work regarding pedestal transport coefficients was performed, that led to the decision to set $\alpha_c = 1.8$. This part was not directly carried out in this thesis work, and hence is not reported here.

The work done is summarised here. At the beginning, the pellet injection was operated with a feedback scheme, in order to estimate the injection frequency needed to sustain the pedestal. After

that, simulations were solved in which a train of pellets was launched keeping fixed the frequency previously obtained. Then, a comparison between the two cases was carried out.
Later, deposition profiles for the three pellet configurations were simulated and evaluated, in order to establish if the local density increment overcomes the 20 % of the pre-injection level. At the end, the fast ions contribution to ablation is evaluated, since the presence of accelerated neutrals (due to NBI) made it necessary to consider their impact in every simulation.
The starting case was a steady state with gas puffing as fuelling method with ETB + ELMs(α_c) recipe.

5.2.1 Feedback model and fixed frequency

After turning off the gas puff, the first step was to carry out integrated simulations in which JETTO was run in combination with the QLKNN transport model and a feedback mechanism for pellet injection. Following this scheme, the injection frequency dynamically varies such that a pellet is launched every time the density drops below a density target decided by the user [44]. Reasonably, this value was set to $n^T_{e,TOB}$.
The pellet parameters (r, v_p, atomic weight) and injection time need to be specified in the first line of the pellet settings panel in JETTO. The atomic weight was always set to $2\ a.m.u.$ (deuterium weight), while the injection time, which represents the instant in which the injector is activated, was made to coincide with the beginning of the simulation.
The results of these simulations, concerning the variation of the top density over time for the three pellet types, are displayed in figure 5.8. It is clear that the density target of $1.4 \cdot 10^{20}\ m^{-3}$ (red line) is sustained for each configuration and the steady state is achieved in the three cases. Reasonably, different pellet sizes led to different injection frequencies, since a smaller number of particles injected leads to a slighter density increment. In particular, the optimized frequencies evaluated in these simulations are $\sim 50\ Hz$, $\sim 17\ Hz$, and $\sim 10\ Hz$ for $r = 0.7\ mm$, $r = 1\ mm$, and $r = 1.3\ mm$, respectively.
The next step was to compare these results with the density profiles obtained in simulations where the injection frequency was kept constant and equal to the value came out from the model in feedback. The results for $r = 1\ mm$ are shown in figure 5.9.

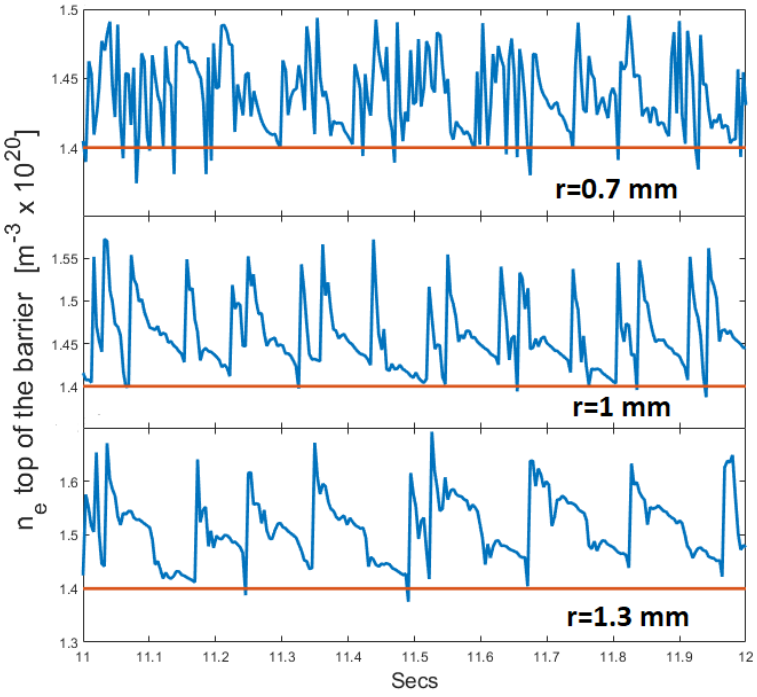

Figure 5.8: Simulations of a pellet fuelled plasma with JETTO equipped with the QLKNN transport model, continuous(α_c) ELMs and feedback pellet injection. Starting from the top: $n_e(TOB)$ variation over time for r=0.7 mm, r=1 mm, and r=1.3 mm.

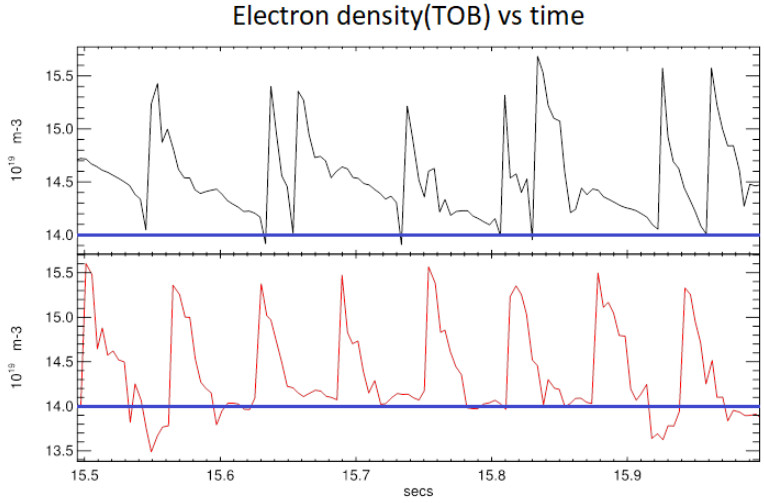

Figure 5.9: Pellet size: $r = 1\,mm$. Top: $n_e(TOB)$ over time in a feedback scheme. Bottom: $n_e(TOB)$ over time for a fixed optimized frequency.

It can be seen that the optimized injection frequency estimated in the first case is effectively suitable to sustain the pedestal in cases in which the injector does not work with a feedback scheme (real cases).

Following the results obtained, a proper fuelling would require an injection frequency up to $\sim 50\,Hz$, well in line with the capacity of present day centrifuge injectors.

5.2.2 Density profile evolution in one pellet cycle

In this section, results concerning density profile evolution due to the pellet injection are presented. Indeed, studying the temporal dynamics of deposition profiles is crucial for many issues.

Firstly, it allows to assess if the local density perturbation due to the pellet injection is less than 20 % of the pre-injection level. Furthermore, it makes possible to evaluate parameters related to fuelling performance, such as the maximum deposition depth ρ_{max} and the penetration depth ρ_{dep}. Ultimately, the density profile evolution permit to investigate on a possible "pile-up" of particles in the plasma core. The results, obtained with JETTO equipped with the QLKNN model, continuous(α_c) ELMs and feedback pellet injection, are displayed in figure 5.10, 5.11, and 5.12.

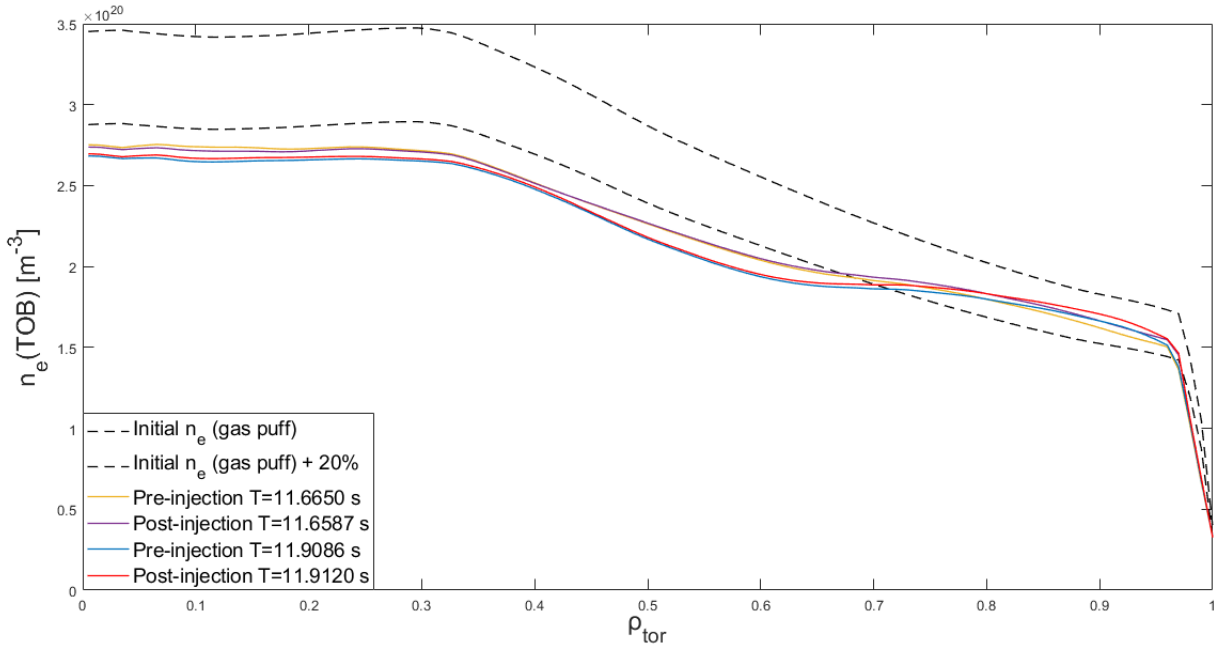

Figure 5.10: Density profile evolution for pellets with r=0.7 mm.

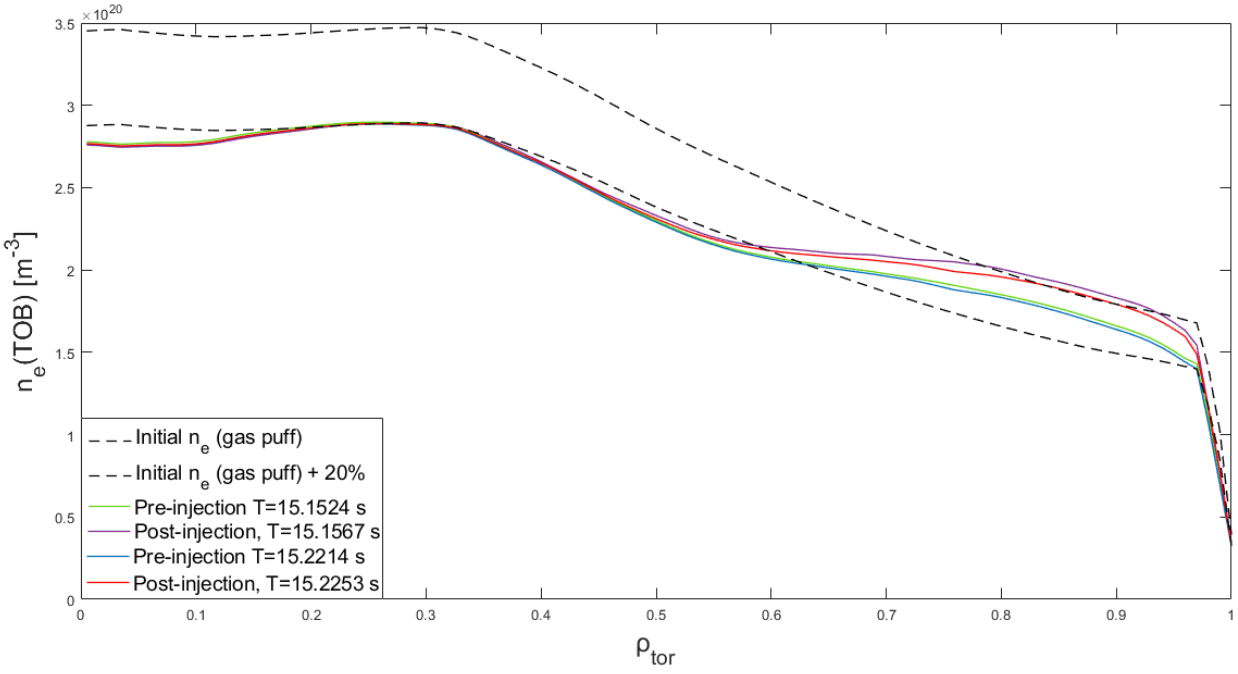

Figure 5.11: Density profile evolution for pellets with r=1 mm.

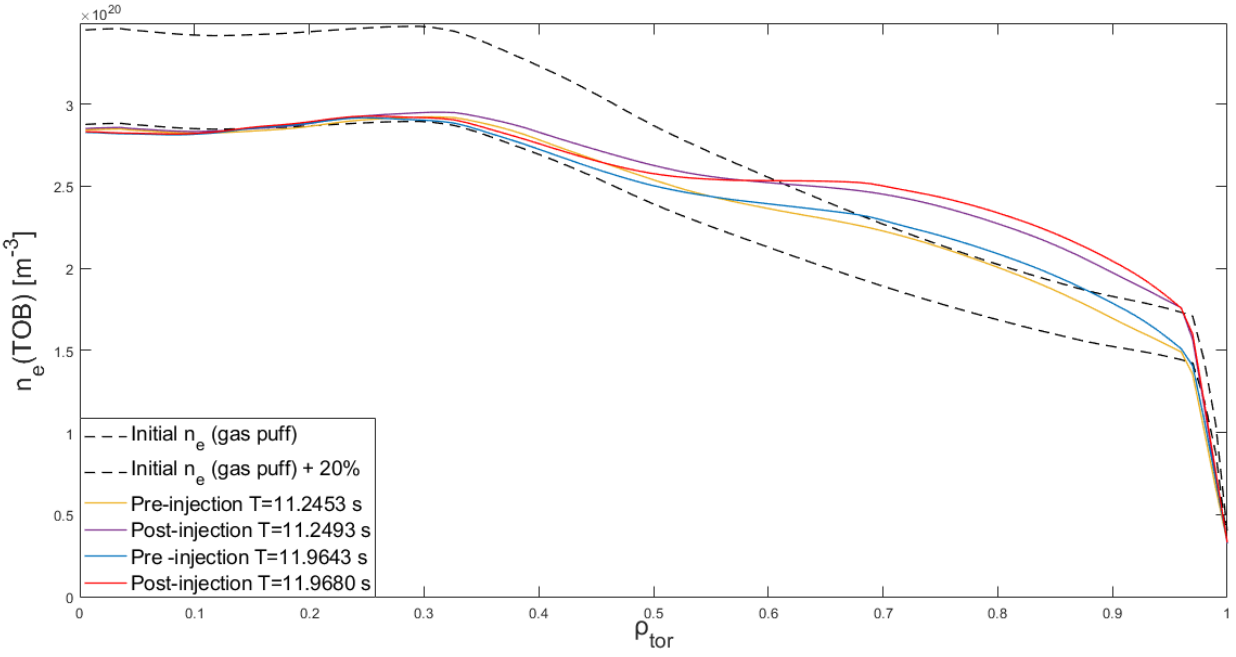

Figure 5.12: Density profile evolution for pellets with r=1.3 mm.

It can be seen that in none of the cases the density profile completely relaxes before the subsequent pellet injection, since the pre-injection value is always above the bottom dashed black

line taken as initial density reference. Nevertheless, launching pellets with these optimized frequencies does not lead to a pile-up, since the density perturbation post-injection remains of the same magnitude regardless of the number of pellets previously inserted.

The density perturbation due to the pellet is less than 20 % of the pre-injection level only for pellets with $r = 0.7\ mm$, while is ~ 20 % for $r = 1\ mm$ and > 20 % for $r = 1.3\ mm$. Therefore, in accordance with the Pégourié report, the density increment is acceptable for pellets with $r \leq 1\ mm$. As we could expect, performance for the third configuration ($r = 1.3\ mm$) seems to be the best since the pellet penetration is significant up to $\rho_{tor} \approx 0.5$, while for pellets with $r = 1\ mm$ and $r = 0.7\ mm$ is remarkable up to ≈ 0.55 and ≈ 0.6, respectively. Moreover, it can be seen that also the maximum penetration depth (depth of the density perturbation peak) increases with the pellet size.

Thus, in light of what these results show, fuelling the DTT plasma via pellets with $r = 1\ mm$ seems to be the fair compromise between fuelling performance and density perturbation constrains.

The conclusions extrapolated from the results shown in both section 5.2.1 and 5.2.2 were validated through subsequent integrated simulations of a pellet fuelled plasma with JETTO equipped with the more complete QLK turbulent transport model. In particular, as displayed in figure 5.13, we obtained a very similar behaviour for local density perturbation up to $\rho_{tor} \approx 0.5$, and hence very similar fuelling performance. Moreover, figure 5.14 shows that also the injection frequencies required to sustain the pedestal are very similar, proving again that QLKNN represents a good test for QLK simulations.

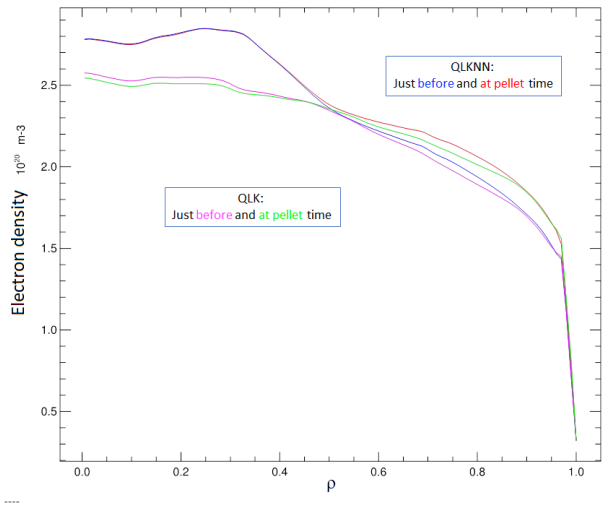

Figure 5.13: Deposition profile performed by QLKNN and QLK.

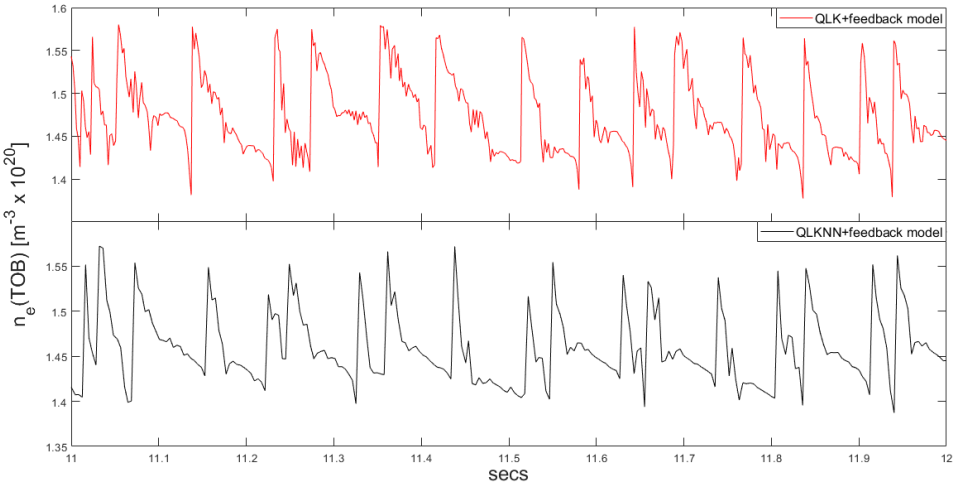

Figure 5.14: Top: JETTO+QLK. Bottom: JETTO+QLKNN.

Ultimately, in order to evaluate the fast ions contribution to the ablation process, a pellet deposition profile was obtained by running the HPI2 code without fast particles. The result was then compared to the corresponding case (i.e. same pellet size and velocity) with fast ions, as shown in figure 5.15.

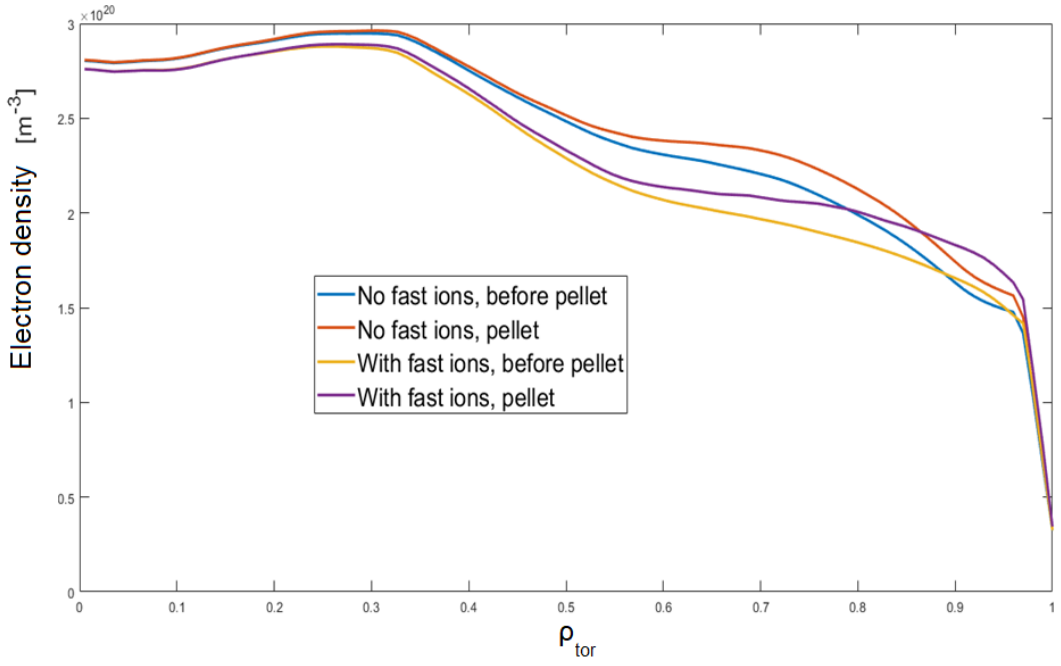

Figure 5.15: Fast ions contribution to ablation. Pellet with $r = 1\ mm$.

It can be seen that fast ions are responsible for a strong over-ablation since the pellet penetrates less into the plasma core and the density presents a slighter perturbation, in accordance with [45].

5.3 Predictive simulations in the new DTT configuration

As pointed out at the end of the fourth chapter, the integrated modelling to which my thesis work belongs led to the decision to enlarge the DTT device up to $R = 2.19\,m$ and $a = 0.70\,m$. Thus, a work of integrated simulation for this new DTT configuration has started, making it necessary to repeat the tuning of the pedestal with gas puff as fuelling method. In these simulations, values at the separatrix more consistent with a scrape-off layer in the detached state were used, particularly a higher separatrix density.

As in the first case, the work started from reference profiles with the fixed pedestal calculated by the Europed code with the EPED1 model.

Again, the ELM continuous(TOB) model was exploited, using target values in line with the new fixed pedestal levels, as follows:

$$n^T_{e,TOB} = 1.38 \cdot 10^{14}\ cm^{-3}$$
$$T^T_{i,TOB} = 1200\ eV$$
$$T^T_{e,TOB} = 1200\ eV$$

In order to ensure the compatibility between plasma scenarios and first wall power handling capability, the edge modelling in the new DTT configuration highlighted the need to achieve strong SOL radiation by impurity seeding (Ar or Ne) at separatrix density levels $\geq 0.7 \cdot 10^{14}\,cm^{-3}$, making it necessary to raise the boundary conditions in the new FP scenario, as follows:

$$I_p = -5.5\ MA$$
$$T_i = T_e = 130\ eV$$
$$n_e = 0.8 \cdot 10^{14}\ cm^{-3}$$

The work started with the tuning of the ETB. The width and the smoothing of the barrier were varied in order to reproduce the fixed pedestal, while the nominal gas puff rate was kept constant at $3 \cdot 10^{22}\,s^{-1}$. As in the first case, the neutral particle input was modelled by FRANTIC using a feedback mechanism, and the turbulent transport model QLK was exploited over the whole profile (i.e. up to $\rho_{tor} = 1$). The tuning work of the pedestal parameters led to the decision to set RHONTOB=0.97 and SMTHRHON=0.013. The results are reported in figure 5.16 and 5.17.

It can be seen that these integrated simulations accurately reproduce the temperature profiles with fixed pedestal calculated by EPED1. Again, although the predicted pedestal of the density profile is slightly narrower than the fixed one, the choice of these values represents the fair compromise to reproduce the three reference profiles simultaneously.

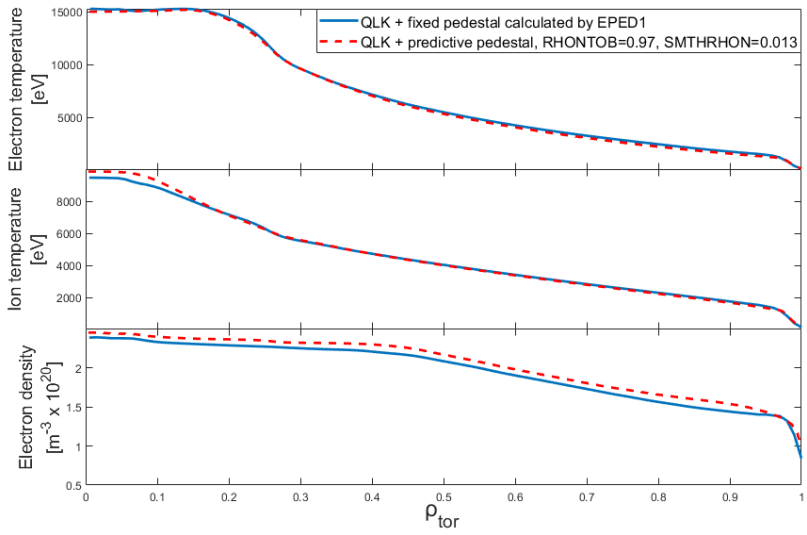

Figure 5.16: Whole radial profile.

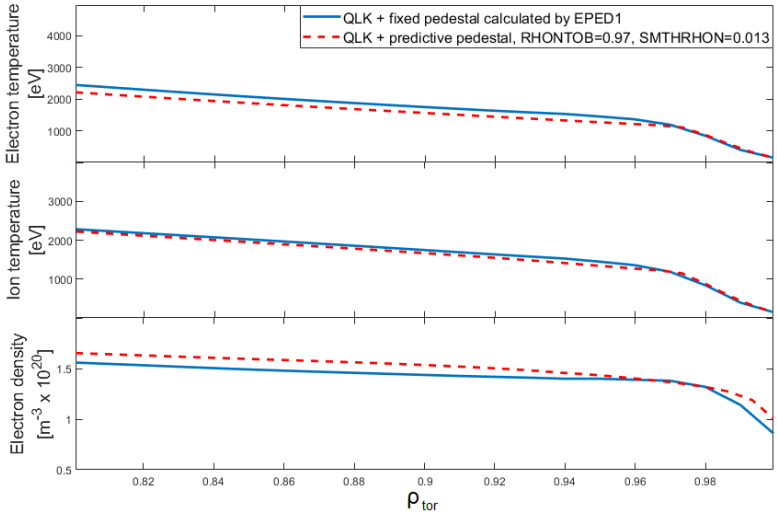

Figure 5.17: Profile zoom in the pedestal region.

The neutral density rate is significant in the pedestal region, although the penetration is smaller than in the case with $R = 2.14\,m$, as shown in figure 5.18.

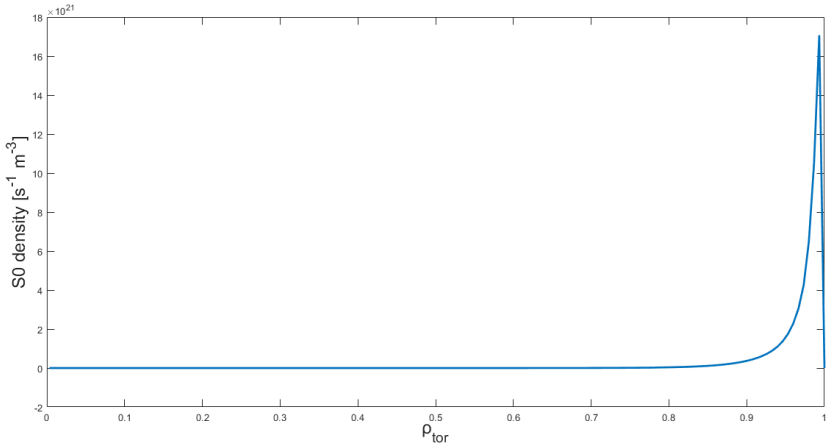

Figure 5.18: Radial profile of the source of neutrals from the edge. PPF number: 2349.

Ultimately, in order to assess if the nominal gas puff rate is higher than the applicability limits, the neutral input source rate is evaluated in figure 5.19.

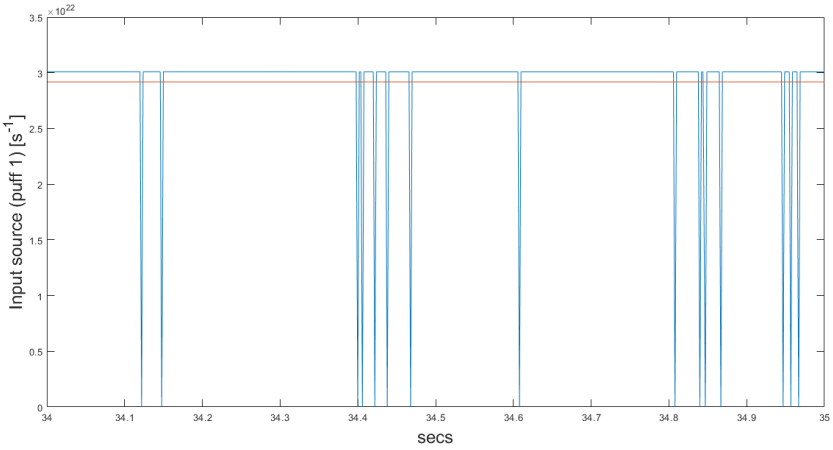

Figure 5.19: Gas puff rate (blu line) and its average value (red line). PPF number: 2349.

It can be seen that a neutral flux level of about $2.9 \cdot 10^{22}$ particles/s at the separatrix is required. As we could expect, this value is significantly higher than the one found in the previous DTT configuration, since the boundary conditions imposed at the separatrix have been raised and the

volume is considerably larger.

In this context, the nominal gas puff rate needed to sustain the pedestal density is remarkably above the feasibility limits for the pumping and puffing systems, making it even more necessary to develop a pellet injection system than in the first configuration.

Chapter 6

Conclusions and future perspectives

In this thesis work, predictive simulations of deuterium fuelling in the DTT plasma using the quasi-linear transport models QLK and QLKNN were carried out. The main purpose was to investigate for the first time the DTT plasma response to the two main particle sources: gas puff and pellet injection, in order to establish the feasibility of these fuelling methods in the Italian project. Firstly, the equations were solved for the previous DTT configuration, with $R = 2.14\,m$ and $a = 0.65\,m$. The results concerning the neutral injection showed that, in order to sustain the desired density levels, high gas puff rates are needed. Since these values are near to the feasibility limit, a pellet injection system is therefore required in order to minimize the operational risk. In particular, the integrated simulations including this second fuelling method showed that pellets with $r \leq 1\,mm$ are a proper alternative to gas puff, since the optimized injection frequency is well in line with injector capacities and the post-injection density perturbation remains below the critical values.

Subsequently, since the integrated modelling to which this thesis belongs led to the decision to enlarge the device up to $R = 2.19\,m$ and $a = 0.70\,m$, it was necessary to repeat the predictive simulations of the gas puff fuelling of the DTT plasma. In these simulations, values at the separatrix more consistent with a scrape-off layer in the detached state were used, particularly a higher separatrix density. As a consequence, the results showed that the neutral flux level required at the separatrix is too high if compared to the feasibility limits.

Thus, it will be required to study and optimize a pellet fuelling system also in this new configuration, making it necessary to repeat the work of predictive simulations in order to evaluate the plasma response to the pellet source.

Bibliography

1. Albanese R et al. *Design review at the Italian Divertor Tokamak Test facility* (Fusion Engineering and Design 146, 194-197, 2019).

2. https://www.dtt-project.enea.it.

3. Freidberg J *Plasma Physics and Fusion Energy* (Cambridge: Cambridge University Press, 2007).

4. Pucella G and Segre S *Fisica dei plasmi* (Zanichelli, 2009).

5. Wesson J *Tokamaks* (Oxford University Press, 2004).

6. Boyd T J M *The Physics of Plasmas* (Cambridge: Cambridge University Press, 2003).

7. Horton W et al *Drift waves and transport* (Rev. Mod. Phys. 71:735-778, Apr 1999).

8. Garbet X and Mantica P *Physics of transport in tokamaks* (Plasma Physics and Controlled Fusion 46(12B):B557-B574, nov 2004).

9. Rechester A B et al *Electron Heat Transport in a Tokamak with Destroyed Magnetic Surfaces* (Physical Review Letters 40 (1978) 38).

10. Weiland J *Collective Modes in Inhomogeneous Plasma* 2000.

11. Romanelli F et al *The radial structure of the ion-temperature-gradient-driven mode* (Physics of Fluids B: Plasma Physics, 5(11):4081-4089, 1993).

12. Jenko F et al *Electron temperature gradient driven turbulence* (Physics of Plasmas, 7(5):1904-1910, 2000).

13. Kadomtsev B B et al *Trapped particles in toroidal magnetic systems* (Nuclear Fusion, 11(1):67-92, jan 1971).

14. Mantica P et al *Progress and challenges in understanding core transport in tokamaks in support to ITER operations* (Plasma Phys. Control. Fusion 62, 014021).

15. Brizard A J et al *Foundations of nonlinear gyrokinetic theory* (Rev. Mod. Phys., 79:421-468, Apr 2007).

16. Gorler T et al *The global version of the gyrokinetic turbulence code GENE* (Journal of Computational Physics, 230(18):7053-7071, 2011).

17. Staebler G M et al *A theory-based transport model with comprehensive physics* (Phys. Plasmas 12, 102508, 2005).

18. Bourdelle C et al *A new gyrokinetic quasilinear transport model applied to particle transport in tokamak plasmas* (Phys. Plasmas 14, 112501, 2007).

19. Bourdelle C et al *Core turbulent transport in tokamak plasmas: bridging theory and experiment with QuaLiKiz* (Plasma Phys. Control. Fusion 58, 014036, 2016).

20. Bourdelle C at al *Stability analysis of improved confinement discharges: internal transport barriers in Tore Supra and radiative improved mode in TEXTOR* (Nucl. Fusion 42 892, 2002).

21. Tamor S at al *ANTIC: A code for calculation of neutral transport in cylindrical plasmas* (Journal of Computational Physics 40, 104-119, 1981).

22. Garzotti L at al *Neutral gas and plasma shielding scaling law for pellet ablation in Maxwellian plasmas* (1997 Nucl. Fusion 37 1167).

23. Lengyel L L at al *Pellet ablation in hot plasmas and the problem of magnetic shielding* (Phys. Fluids 21, 1978).

24. Pégourié B at al *Homogenization of the pellet ablated material in tokamaks taking into account the* ∇B*-induced drift* (Nucl. Fusion 47 44, 2006).

25. Pégourié B et al *Neutrals and impurities model and pumping* (2020).

26. Romanelli M et al *JINTRAC: A System of Codes for Integrated Simulation of Tokamak Scenarios* (Plasma Fusion Res. 9 3403023, 2014).

27. Lao L L et al *Separation of β_p and l_i in tokamaks of non-circolar cross-section* (Nucl. Fusion 25 1421, 1985).

28. Albanese R et al (ISEM (2003), Versailles, pp.404-405).

29. Cenacchi G et al *JETTO: A Free-boundary Plasma Transport Code* (JET Joint Undertaking, 1988).

30. Taroni L et al (Proc. 21st EPS I, 102, 1994).

31. Romanelli M et al *Effects of density asymmetries on heavy impurity transport in a rotating tokamak plasma* (Plasma Physics and Controlled Fusion, 40(10):1767-1773, oct 1998).

32. Eriksson L G et al *Comparison of time dependent simulations with experiments in ion cyclotron heated plasmas* (Nuclear Fusion, 33(7):1037, 1993).

33. Challis C D et al *Non-inductively driven currents in JET* (Nuclear Fusion, 29(4):563, 1989).

34. Farina D et al *A Quasi-Optical Beam-Tracing Code for Electron Cyclotron Absorption and Current Drive: GRAY* (Fusion Science and Technology, 52(2):154-160, 2007).

35. Hirshman S P et al *Bootstrap current and neoclassical transport in tokamaks of arbitrary collisionality and aspect ratio* (Physics of Plasmas, 4(9):3230-3242, 1997).

36. Hogan J T et al (Nucl. Fusion 19, 753, 1979 and ORNL/TM - 6409 Report ,1978).

37. Zohm H et al *Edge localized modes (ELMs)* (Plasma Phys. Control. Fusion 38, 105–128, 1996).

38. Garzotti L et al *Simulations of density profiles, pellet fuelling and density control in ITER* (Nucl. Fusion 52, 2012).

39. Casiraghi I et al *First-principle based multi-channel integrated modelling in support to the design of the Divertor Tokamak Test facility* (Nucl. Fusion, 2021).

40. Saarelma S et al *Integrated modelling of h-mode pedestal and confinement in JET-ILW* (Plasma Physics and Controlled Fusion, 60, nov 2017).

41. Snyder P B et al *A first-principles predictive model of the pedestal height and width: development, testing and ITER optimization with the EPED model* (Nuclear Fusion 51, aug 2011).

42. van de Plassche K L et al *Fast modeling of turbulent transport in fusion plasmas using neural networks* (Physics of Plasmas 27, 2020).

43. Balbinot L et al *Development of DTT single null divertor scenario* (Nuclear Materials and Energy, 27:100952, 2021).

44. Bufferand H et al *Near wall plasma simulation using penalization technique with the transport code SolEdge2D-Eirene* (Journal of Nuclear Materials, 438:S445-S448, 2013. Proceedings of the 20th International Conference on Plasma-Surface Interactions in Controlled Fusion Devices).

45. JINTRAC TEAM (JETTO wiki, JETTO Extra Namelists documentation).

46. Pégourié B et al *Modelling of pellet ablation in additionally heated plasmas* (Plasma Phys. Control. Fusion 47 17, 2004).